

# Numerical study of the influence of ion-induced electrons on the dynamics of electron clouds in gyrotron-like geometries

S. Guinchard\*

*Section de Physique, Ecole Polytechnique Fédérale de Lausanne, Lausanne, Suisse*

(Supervised by G. Le Bars and J. Loizu)<sup>†</sup>

(Dated: January 15, 2023)

In this document, the influence of ion-induced electron emissions (IIEE) on the formation of electron clouds in several gyrotron-like geometries is reviewed. Results are compared to the case without taking account for IIEE. The implemented geometries correspond to electrode designs from the TREX experiment [RAH<sup>+</sup>22], currently being built on site at EPFL. The results are obtained by mean of the highly parallelised FENNECS code [LB22], in which a module was implemented to deal with these IIEE. Finally, a cloud formation study is conducted in the refurbished geometry from the gyrotron GT-170, part of the ITER plan for ECRH.

**Keywords:** Gyrotron, IIEE, ion-induced electron emissions, FENNECS, TREX, Magnetron Injection Gun, GT-170, magnetic potential well, trapping, electron trapping

## I. INTRODUCTION

Over the years, the energy needs have not stopped increasing at a global scale, and the diminishing fossil fuels ressources, as well as ecological concerns, have made emerge new sources for a sustainable energy production. Nuclear fusion is among them. The research in nuclear fusion is a tremendous task that has kept physicists busy for years now. For a nuclear fusion power plant to operate, various complex systems have to work together, as the plasma need to be produced, heated and confined. Plasma heating is an important field of research, since an optimized heating system is among the keys to reduce the energy consumption and raise the fusion gain factor  $Q$ .

In the past decades, gyrotrons have proven to be essential devices to reach required conditions for nuclear fusion, as they are used for plasma heating and current drive applications, in a long-pulse or continuous operating mode [Fis87]. They are complex devices made of an ensemble of subsystems, each of them being essential for the functioning, and making intervene their own physical phenomena [OHA<sup>+</sup>11]. It is hence essential for each part to function properly, for the whole heating system to be efficient. One particular part of the gyrotron is of interest, since perturbative phenomena can occur as it is used: the so called MIG, or Magnetron Injection Gun. This system is used to produce the electron beam that will later be used to generate millimeter electromagnetic waves. These waves will resonate with the plasma electrons to heat the latter, or induce a toroidal current, that, in Tokamak, will help generating the poloidal magnetic field indispensable for confinement. It has been shown that various phenomena can disrupt the proper operating mode of the MIG, among which the formation of trapped electron clouds [LBHL<sup>+</sup>22]. These electron clouds can considerably affect the local electric field, and be responsible for currents that make the power-supply sustaining impossible over sufficient times. It is then in our best interest to understand the formation of these clouds, how it depends on the MIG geometry, to be able to prevent their formation, or neutralise them. With this report, we hope to bring additional information on the knowledge about the formation of electron clouds, as a particular phenomenon, the ion-induced electron emissions, is newly considered.

A brief introduction about the functioning of a gyrotron in general, as well as an explanation on the MIG mode of operation and the trapping phenomena that can occur in the latter, leading to the formation of electron clouds, are present in II A. The Trapped Electrons eXperiment TREX and why it is of importance in the context of the trapping of electron clouds is described in II B. A description of the code used to model the electron trapping through solving the collisional Vlasov-Poisson, FENNECS, is detailed in II C. The main theoretical considerations regarding Ion-Induced Electron emissions IIEE, as well as the choice of a relevant model for them, are presented in II D. The details of the numerical implementation of the IIEE as an additional module for the FENNECS code are shown in II E. Finally, the module robustness is tested in III A. Regarding the formation of electron clouds and the influence of IIEE on the latter is treated in III B, in several geometries, including the GT170 MIG from the ITER gyrotrons.

---

\* salomon.guinhardt@epfl.ch

<sup>†</sup> Swiss Plasma Center, Ecole Polytechnique Fédérale de Lausanne, Lausanne, Suisse

## II. THEORY

### A. Gyrotron guns and trapping phenomena

Gyrotrons are microwaves generator devices used in plasma heating and current drive applications for fusion purposes [PPZ<sup>+</sup>16]. The operating mode of gyrotron guns is based on the electron cyclotron maser instability (CMI). This instability occurs when a beam of relativistic electrons, gyrating around magnetic field lines, interact with the transverse component of the electric field. The transverse electrons' energy is then converted in electromagnetic waves in an open, resonant cavity. More precisely, the interaction takes place between the electron beam and a transverse electric mode  $\text{TE}_{m,p,q}$  supported by the cavity, see Fig.(1) - Left. The subscripts  $m, p, q$  denote respectively the azimuthal, radial and longitudinal mode numbers. When the pulsation of the EM wave inside the cavity equals the relativistic electron cyclotron (EC) frequency, that is  $\omega = \omega_e/\gamma$ , a group of electrons with initially no phase relation, will, under the action of the field, regroup and gyrate in phase, as a whole. This is called 'phase bunching', see Fig.(1) - Right. Note that we define  $\omega$ ,  $\omega_e$  as the EM wave and the EC frequencies respectively, and  $\gamma$  the Lorenz factor. Then, increasing the frequency  $\omega$ , after an integer number of periods, the electrons will be in a region such that their transverse velocity is on average positive,  $\langle v_x \rangle > 0$  [Alb91]. Using that the electrons energy  $W$  varies as  $dW/dt = -|e|v_x E_x$ , the energy variation is negative, and by conservation, the latter is converted in EM energy.

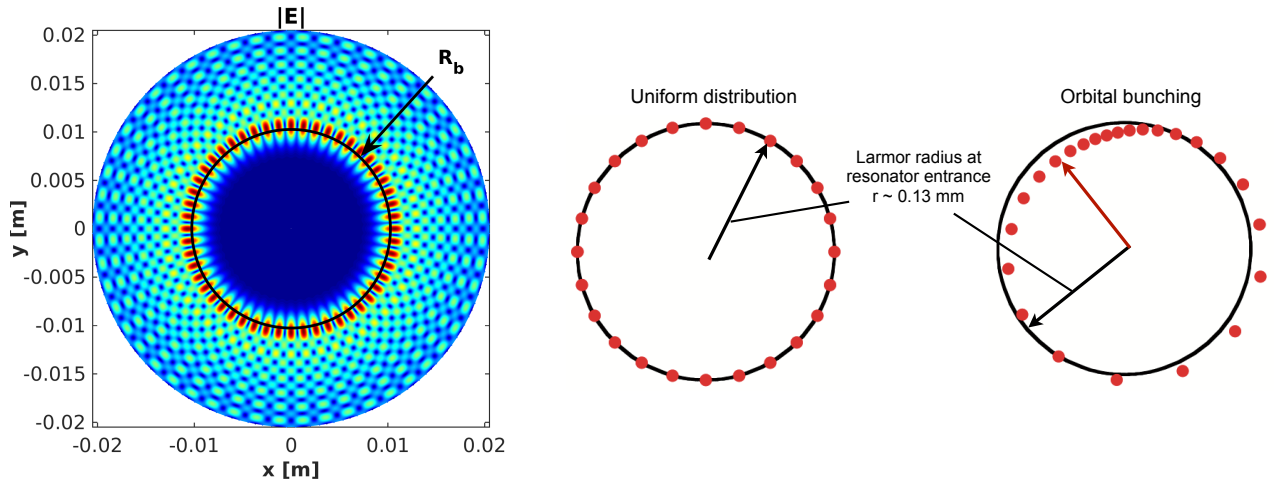


FIG. 1. Left: Amplitude of the electric field profile in the transverse cross-section for the mode  $\text{TE}_{26,7}$  of Tokamak à Configuration Variable (TCV) dual-frequency gyrotron [Gen19]. The black circle represents the annular electron beam. - Right: Orbital bunching mechanism of electrons in the cavity (resonator). Electrons are shown by red dots, and the black circle corresponds to a Larmor orbit. Source: courtesy of S. Alberti.

On top of the cavity lies a mode converter so that the frequency of the emitted microwaves matches one of the plasma resonance frequencies. The radiation is then reflected by several mirrors and directed through a diamond window so it can penetrate the plasma, see Fig.(2). The most common heating frequency corresponds to the electrons' gyrofrequency  $\omega_e$ , or some of its harmonics. In that case, we speak of electron cyclotron resonance heating (ECRH). It is when the electromagnetic wave has a component along the toroidal magnetic field that it can induce a current. The latter phenomenon is called electron cyclotron current drive (ECCD).

All the previously described events occur in the gyrotron cavity, or after the latter. However, the beam quality as it enters the cavity is very important, since it will, among others, participate to the interaction efficiency [PPZ<sup>+</sup>16]. The beam is generated by an electron gun, also called magnetron injection gun (MIG). An axial cross section of the MIG is depicted in the left part of Fig.(2). It consists in a cylindrical cathode around a coaxial insert, and a cylindrical anode of a larger radius around it. The beam electrons are produced by thermo-emission. The electrons are accelerated by the electric field and guided through the exit of the MIG by mean of the magnetic field present as shown in Fig.(2), so they can reach the cavity where they will achieve the collective gyro-motion from the CMI. Nevertheless, multiple phenomena can disrupt the functioning of the MIG, among which the formation of trapped

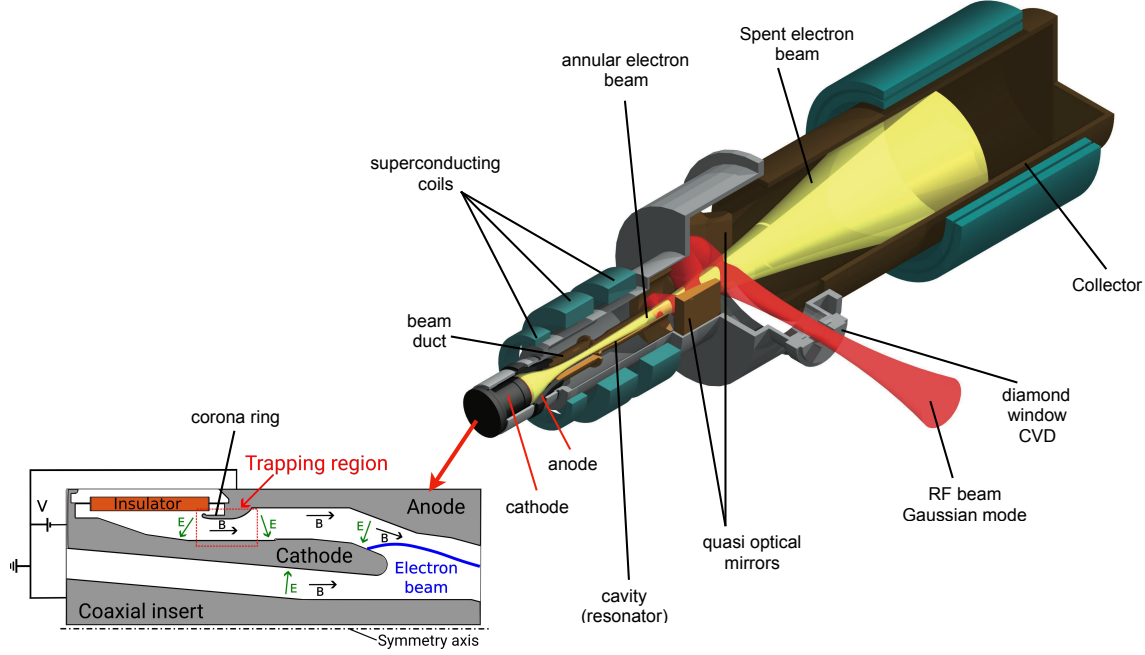


FIG. 2. Right: Schematic of a gyrotron gun and its different constituents. Source: courtesy of S. Alberti - Left: Zoomed view of the MIG from the gyrotron [RAH<sup>+</sup>22].

electron clouds in the rear part of it [PPZ<sup>16</sup>, LBHL<sup>22</sup>]. Indeed, as the local population of electrons increase inside the MIG cavity, discharges phenomena can occur when a certain critical value is reached. Thus, voltage stand-off problems can follow from discharges [HGA<sup>09</sup>], that were later attributed to the presence of these trapped electrons. Regarding the trapping in itself, electrons can accumulate in a cloud for several reasons, as among others, the so-called adiabatic trap, or the potential well trap. In this report, we will focus on the second. Let us first briefly summarise this type of trapping mechanism.

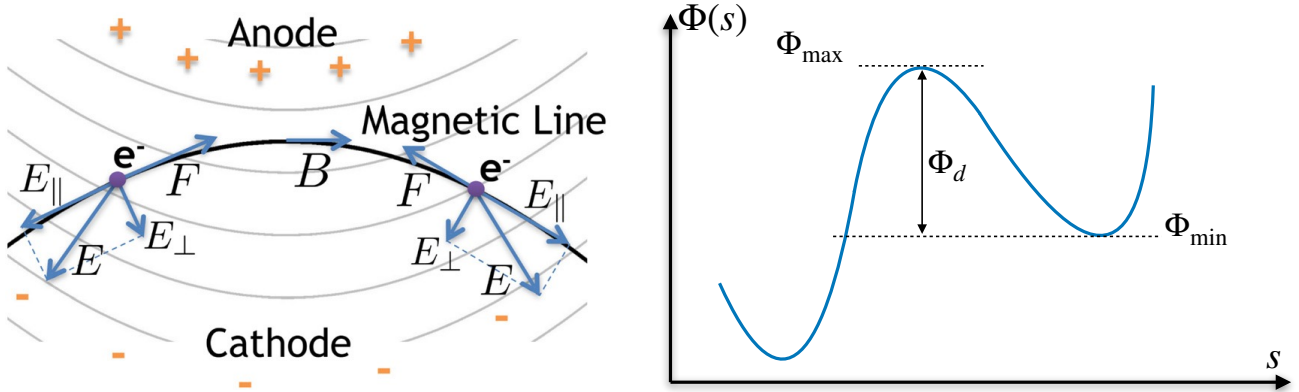


FIG. 3. Left: configuration favorable to the formation of a potential well. The equipotentials are depicted by plain, grey lines, while the magnetic field line is represented by the black one [PPZ<sup>16</sup>] - Right: Potential-well definition. The curvilinear abscissa along the field line is denoted by  $s$ .

A magnetic potential well can form every time a magnetic line intersects twice an equipotential as depicted in Fig.(3). Indeed, in such a configuration, the electrons are accelerated on one side of the well and decelerated on the other side by the Coulomb force projected along the field line  $F_{||} = -eE_{||}$ . The potential well is characterised by its location as well as its depth, which is defined locally as the difference between the local maximum  $\Phi_{max}$  and the highest of the local minima on both side of  $\Phi_{max}$ . Hence, the depth reads  $\Phi_d = \Phi_{max} - \max \{\Phi_{min}\}$ . Thus, the electrons

oscillate inside that well around its center, while the component  $E_{\perp}$  of the electric field contributes to an azimuthal drift  $\mathbf{v}_d \propto \mathbf{E}_{\perp} \times \mathbf{B}$ , causing the electrons to gyrate around the MIG symmetry axis, giving the cloud an annular shape.

### B. TRapped Electrons eXperiment TREX

In order to emphasize experimentally the mechanism of electron trapping by magnetic potential well as described in II A, an experiment is, at the time of writing, being built at the Swiss Plasma Center (SPC) [RAH<sup>+</sup>22]. The TREX experiment aims at studying the formation of electron clouds under multiple gyrotron's magnetic, electric and neutral pressure configurations. One sees indeed that the outer electrode designed as shown in Fig.(4) is an approximate replica of the corona-ring from MIG.

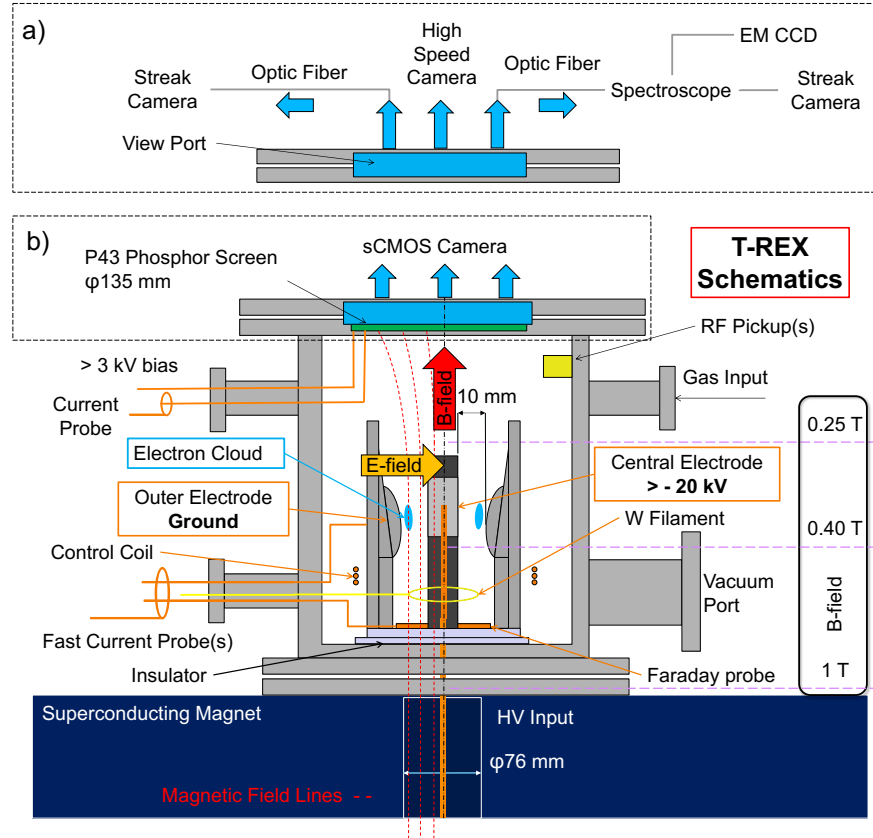


FIG. 4. Schematic of the TREX experiment [RAH<sup>+</sup>22].

Regarding the experiment design in itself, the chamber is set on top of a superconducting magnet, such that the magnetic field lines run through the chamber axially. The potential bias between the two electrodes is planned to be of about  $\Delta\Phi = 20$  kV and the electric field topology is changed locally by mean of amovible and interchangeable electrodes. The magnetic field intensity is kept between 0.25 – 1.0 T, and the neutral pressure should range as  $p = 10^{-7}$  to  $10^{-5}$  mbar. A tungsten filament can act as a source of electrons, although it has been shown by [LBHL<sup>+</sup>22] that background radiation could be sufficient in certain geometries, to provoke the formation of a cloud. The optical diagnostic methods consist in either a sCMOS camera on top of a biased phosphor screen, or streak camera working together with a high speed camera as well as a spectroscope. When neutralising the cloud by switching off the high-voltage source, the cloud would follow the field line and be directed towards the phosphor screen, enabling to measure the current through it, and the image would be taken by the sCMOS camera. The experiment being built currently, the design is guided by some FENNECS code results, and some numerical characteristics as the expected cloud density were deduced from simulations too. The experimental results are to be confronted to the code ones.

### C. The FENNECS code

In order to model the electron trapping in various geometrical situations, the FENNECS code [LB22] was used. It is a 2D3V particle-in-cell code, that solves the Poisson-Vlasov system from Eq.(1) in cylindrical geometry, for the distribution function  $f_e$  and the electrostatic potential  $\phi$ . It has been developed in order to show the self-consistent formation of electron-clouds in gyrotron guns, due to the ionisation of the residual neutral gas (RNG) present in the gyrotron cavity [LBHL<sup>+</sup>22].

$$\begin{aligned} \left( \frac{\partial}{\partial t} + \mathbf{v} \cdot \frac{\partial}{\partial \mathbf{x}} + \frac{e}{m_e} (\mathbf{E} + \mathbf{v} \times \mathbf{B}) \cdot \frac{\partial}{\partial \mathbf{v}} \right) f_e(\mathbf{x}, \mathbf{v}, t) &= 0, \\ \nabla^2 \Phi(\mathbf{x}, t) &= -\frac{e}{\epsilon_0} \int f_e(\mathbf{x}, \mathbf{v}, t) d^3 \mathbf{v}. \end{aligned} \quad (1)$$

FENNECS is a highly parallelised code in the sense that it uses both multiple nodes (MPI) and multiple core per node (openMP). Regarding numerical methods, the code uses cylindrical coordinates, and axisymmetry is assumed, so that  $\partial_\theta = 0$ ,  $\theta$  being the poloidal coordinate. The poisson equation is solved using finite elements, based on weighted extended b-splines, whereas the collisional Vlasov equation is solved by sampling the electron distribution  $f_e$  with macro-particles, then calculating the trajectory of each macro-particle by mean of the Boris algorithm [LBHL<sup>+</sup>22, BLVV85]. So far, the code only takes account for primary ionisations coming from electron-neutral collisions, where electrons collide with the RNG. In fact, the ions having a Larmor radius of the order of the meter, they are collected at the cathode, during times much shorter than the average ionisation time. Indeed, being generated with approximately zero velocity (the RNG atoms have zero velocity in the code), the ions characteristic 'living' time is roughly  $\tau_l \sim \Delta r / v_{\mathbf{E} \times \mathbf{B}}$ ,  $\Delta r$  being of the order of the distance between the electrodes ( $\sim$ cm), which is much shorter than the ionisation time. Taking  $B \sim 0.2$  T,  $\Delta\Phi \sim 2 \cdot 10^4$  V and  $\Delta r \sim 10^{-2}$  m, with  $\Delta\Phi$  the electrostatic potential bias between the electrodes, one gets that  $\tau_l \sim 10^{-9}$  s. Although this estimate is very rough, for a pressure of  $10^{-6}$  mbar, characteristic of gyrotron guns, the ratio of the ions living time to the characteristic ionisation time is of about  $\tau_l/\tau_{io} \sim 10^{-6}$  [LBHL<sup>+</sup>22]. Thus, the ions-neutrals collisions are neglected, and the electrons-neutrals collisions are implemented using a Monte-Carlo method.

However, although ions-neutral collisions are neglected in the ionisation process, the ions contribution in the formation of electron-clouds can be non-negligible, since when they impinge on the cathode, some electrons can be generated at the metallic surface, by various emission phenomena [Bar93]. The ion-induced electron-emissions will be the object of the following study, having first to be implemented in the code, before to be compared with situations where electron clouds form self-consistently, without taking account for IIEE.

### D. Ion-Induced Electron-Emissions

In order to take into account IIEE in the FENNECS code, the question of choosing the appropriate physical model arose. Indeed, expected energy distribution of the ions in the TREX experiment was ranging between 0 and 20-30 keV. These values correspond to roughly the minimal and maximal values that could be reached by ions accelerated in an electric field perpendicular to the magnetic field lines, in vacuum, and over a distance of about 1cm. Fig.(5) shows the initial distribution of protons in the coaxial geometry with the  $(\mathbf{E}, \mathbf{B})$  configuration described previously, where the electric equipotentials are plotted in blue, and the magnetic field lines in black. In this particular configuration, in vacuum, the acquired energy of the protons when they reach the cathode follows

$$E(r_0) = \Delta\Phi \frac{\log\left(\frac{r_0}{r_a}\right)}{\log\left(\frac{r_b}{r_a}\right)}, \quad (2)$$

where  $r_0$  is the initial proton radial position,  $\Delta\Phi$  the potential bias between the cathode located at  $r_a$  and the anode located at  $r_b$ . Thus, taking numerical values such as  $\Delta\Phi = 20$ kV and evaluating  $E(r_a)$  and  $E(r_b)$ , one get that  $E \in [0, 20]$  keV. This way, a model describing IIEE in this energy range had to be found.

Regarding the model in itself, one had to consider that IIEE would be dependent on the material constituting the electrodes. Indeed, protons impinging on stainless steel would not have the same effect as if they were striking a copper electrode. The electron yield would also depend on the energy of the incident particle. It was expected that the number of released electrons would be different if the ion hit the cathode at high or low energy. At this point,

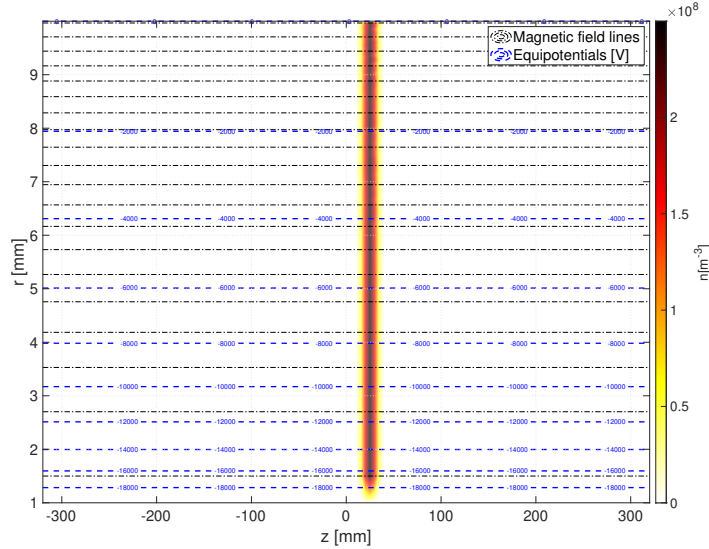


FIG. 5. Initial ion configuration in  $(R, Z)$  plane. The geometry is coaxial. Azimuthal symmetry is assumed.

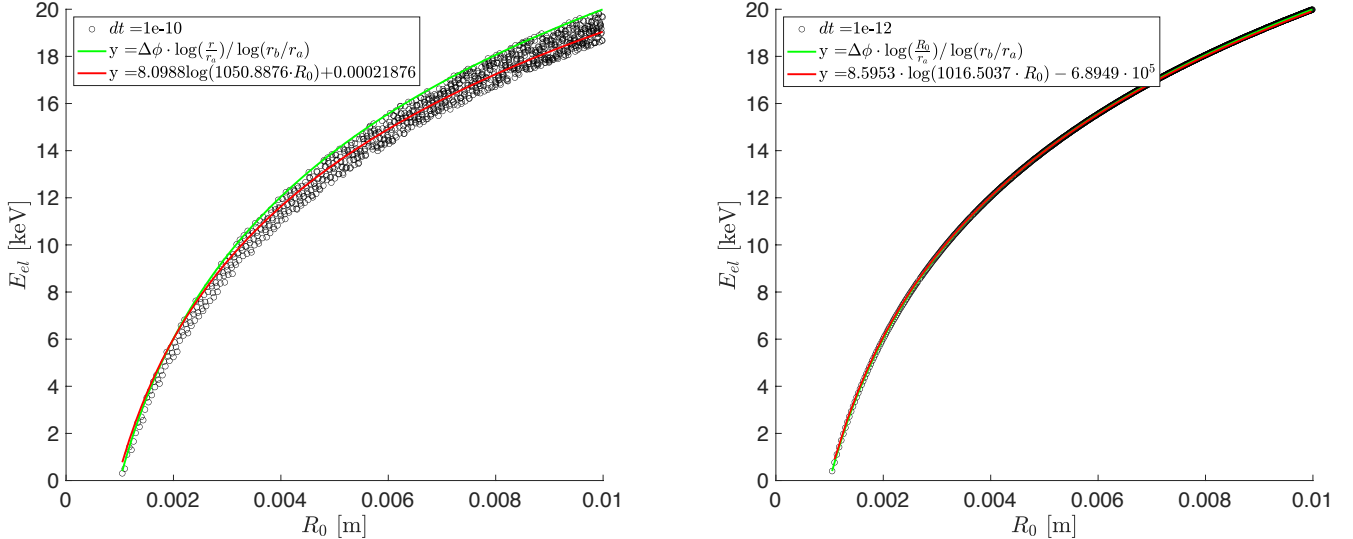


FIG. 6. Left: energy of the collected ions as they hit the cathode,  $dt = 10^{-10}$  s. The red curve is the analytical expression for the energy, corresponding to the vacuum electric potential. The red curve is a fit of the data. - Right: Same with  $dt = 10^{-12}$ .

nothing ensured that the type of interaction between ion and electrode would be the same on the whole energy range. It was also expected that the electron yield would depend on ions parameters: mass  $m$ , charge  $q$  or charge to mass ratio  $q/m$  for example.

With these considerations, one model drew our attention: Schou's model, derived by Schou in 1980. Our motivation for a qualitative (at first) survey of these ion-induced electrons drove us towards this model in particular, since it distinguishes itself by its remarkable simplicity. Following the description of Schou's model from [DH], this approach of IIEE is based on the ionisation cascade theory, and a system of Boltzmann transport equations. Neglecting recoil ionisation in the material, the electron yield  $\gamma$  takes the following form:

$$\gamma = \Lambda \cdot D_e, \quad (3)$$

where  $D_e$  is the amount of energy deposited by inelastic collision **at the surface**, and  $\Lambda$  contains cross sections

dependent parameters for the interaction at a given energy and has the following form

$$\Lambda = \int_0^\infty \frac{\Gamma_m E}{4|dE_i/dx|(E + W)^2} dE. \quad (4)$$

In the above expression for  $\Lambda$ ,  $E = E_i - W$ ,  $\Gamma_m$  is a function of cross-sections and  $W$  a potential barrier term. The term  $dE_i/dx$  corresponds to the energy loss of low-energy electrons in the material. The interesting point of this model is that it is made of two independent terms, one containing target material parameters ( $\Lambda$ ) and the other containing the impacting particle characteristics ( $D_e$ ). Another advantage of this separated description is that it can be reformulated such that it is expressed in terms of the energy loss of the incident particles inside the material, which is a quantity that can be measured easily, and for which tabulated numerical values exist. Thus, denoting by  $dE/dx|_i$  the energy loss of ions in the electrode material, one can write the electron yield as follows:

$$\gamma = \Lambda \cdot \beta \cdot \left. \frac{dE}{dx} \right|_i. \quad (5)$$

In Eq.(5),  $\beta$  accounts for energy transport by recoiling electrons and backscattered ions. It has been shown that the product  $\Lambda \cdot \beta$  is for most metals, independent of the material, and has been measured to be approximately  $10^{-6}$  cm/keV. [DH]. Thus, the model used in our module reads:

$$\gamma = \Lambda_{exp} \cdot \left. \frac{dE}{dx} \right|_i := 10^{-6} \cdot \left. \frac{dE}{dx} \right|_i. \quad (6)$$

One point that it is important to be emphasized, is that Schou's model is a kinetic model that holds for substantially high energies, that is above 1keV. For energies below, Schou's theory has to be replaced by another model, in which kinetic emissions are replaced by the so-called potential emissions.

The potential emissions model that has been chosen to treat ion-induced electron emissions at low energies ( $E < 1\text{keV}$ ) is due to Kishinevsky [Kis73]. The result is very elegant in the sense that it depends only on the Fermi energy of the material, the ionisation energy required to produce the incident ions, and the work function of the metal. Since no energy dependence of the electronic yield arises in this model, it should be **constant** in the range  $[0, 1]$  keV. Comments on the validity of this approximation will be made below. Let us now briefly summarise the derivation of the result for  $\gamma$ . First, let us state the expression for the electronic yield as derived in [Kis73]:

$$\gamma \sim \frac{0.2}{\epsilon_F} (0.8 \cdot E_i - 2\phi), \quad (7)$$

where  $\epsilon_F$  denotes the Fermi energy of the metal constituting the target material,  $\phi$  its work function, and  $E_i$  the ionisation energy required initially to produce the incident ions. For hydrogen, this ionisation energy is  $E_H \simeq 13.6$  eV. To justify this last expression, let us briefly resume the steps followed by Kishinevsky. Hagstrum had identified in [Hag54] that the electron yield induced by potential emissions followed:

$$\gamma := \int_{\epsilon_0}^\infty N_i(\epsilon_K) P_e(\epsilon_K) d\epsilon_K, \quad (8)$$

with  $N_i(\epsilon_K)$  the energy distribution of Auger electrons inside the metal. The energy of the electrons is denoted by  $\epsilon_K$ , and  $\epsilon_0$  is defined as  $\epsilon_0 := \epsilon_F - \phi$ . Note that  $P_e(\epsilon_K)$  is the probability that the electron with energy  $\epsilon_K$  overcomes the potential barrier at the surface of the metal. Studying experimentally the dependence of the yield on several parameters, it has been shown that the yield is a function of only three parameters  $\gamma \equiv \gamma(\epsilon_F, \phi, E_i)$ . Kishinevsky then reviewed yield values at fixed parameters. Fixing  $(\phi, E_i)$ , he managed to show that  $\gamma_{(\phi, E_i)} \simeq \frac{cst}{\epsilon_F}$ . Applying the same procedure for  $\epsilon_F$  and  $E_i$ , he constrained  $\gamma$  as follow:

$$\begin{aligned} \gamma &\simeq \frac{0.23}{\epsilon_F} (0.75 \cdot E_i - 2\phi), \\ \gamma &\simeq \frac{0.18}{\epsilon_F} (0.83 \cdot E_i - 2\phi). \end{aligned} \quad (9)$$

These expressions are very close to each other and for  $E_i > 3\phi$ , they differ by about  $\pm 10\%$  [Kis73]. Hence, still with an accuracy of about 10%, he deduced Eq.(7). Note that this model is semi-empirical.

### E. Numerical implementation

In order to implement numerically Schou's model from Eq.(6), it was necessary to obtain reference values for the electronic yield, as a function of incident ions' energies. Tabulated values for the energy loss  $dE/dx$  of protons in various materials were extracted from [Jan82a, Jan82b]. To be consistent with the TREX experiment plans (See II B), attention was drawn on 304 stainless steel ( $^{304}\text{SS}$ ), copper (Cu) and aluminum (Al).

From the tabulated values for  $dE/dx$  obtained, energy loss curves for protons in various materials were derived, and a primary tendency for the electronic yield appeared. Indeed, for all three materials,  $d^2E/dx^2 < 0$ , that is the energy loss is a concave function of the incident energy, in the range of interest. Since the electronic yield is directly proportional to the energy loss, one deduces that it is increasing yet concave on our restricted ions energy range. Fig.(7) shows the electronic yield from the tabulated values, based on a proportionality constant  $\Lambda_{exp} = 10^{-3} \text{ cm}/\text{MeV}$ . One then remarks that the yield is the highest for  $^{304}\text{SS}$  at higher energies, and lowest for Al.

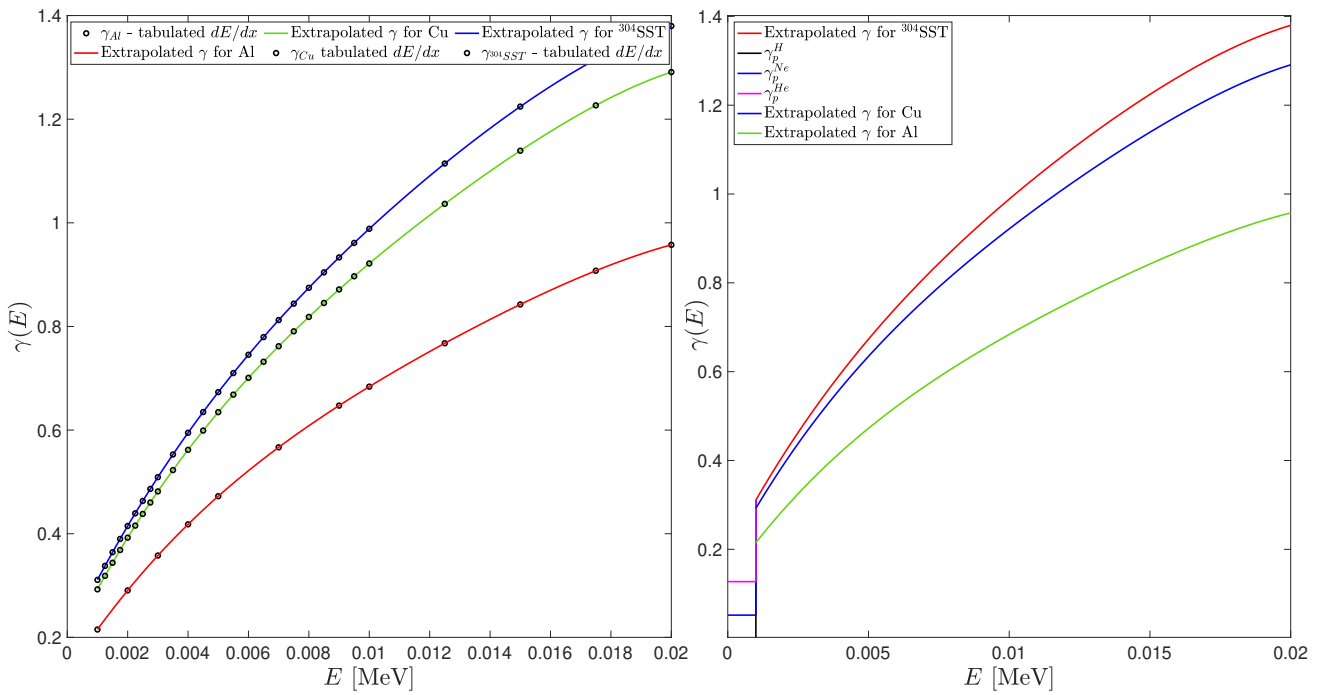


FIG. 7. Electronic yield  $\gamma$  obtained from tabulated values of  $dE/dx$  from [Jan82a, Jan82b] and extrapolated between the points, for the 3 possible electrode materials. Left: Let appear the tabulated values - Right: Extrapolated  $\gamma(E)$  over the full energy range taking account for the potential emissions model (constant yield) from Eq.(7).

To numerically implement the previous results, the yield curve  $\gamma(E)$  had to be polynomially interpolated between the points. Since the required degree for a polynomial fit over the full energy range would have been somewhat too high to be implemented in the code, for numerical complexity reasons, the energy range has been split so that the curve could be fitted by several degree-3 polynomials in the kinetic emissions region, as shown in Fig.(8). Note that quadratic polynomials would have underfitted the curve, while degree 4 polynomials would overfit for the desired precision, and weigh down the numerical treatment. Regarding the potential emissions region, the yield curve was linearly interpolated between the bottom of the kinetic emissions region to the constant value from Kishinevksy's model. Thus the yield curve simply reduced to piecewise polynomials, whose coefficients were implemented in the FENNECS code.

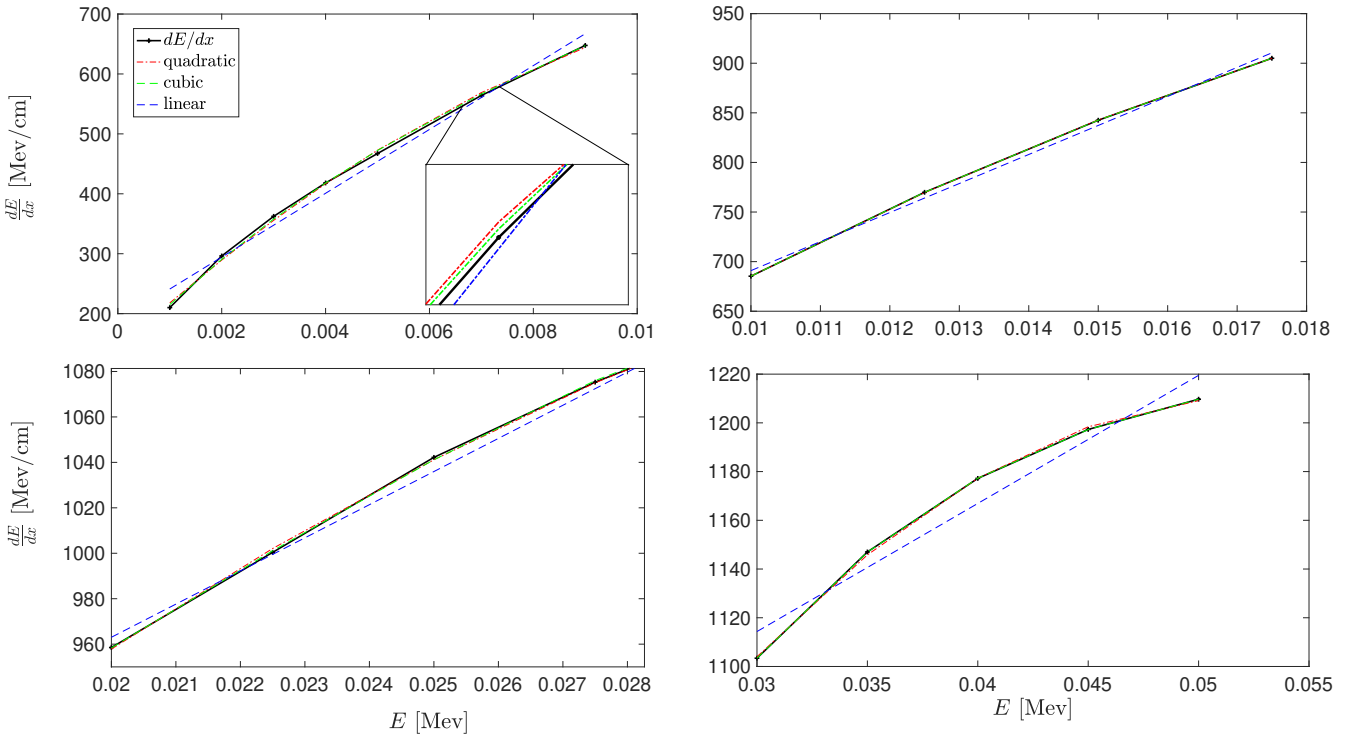


FIG. 8. Several fitting polynomials for the energy loss curve  $dE/dx$ , over the kinetic energy range. For all four intervals, the best fitting was, as shown in the zoom part of the first plot, cubic.

Regarding the emission of electrons in itself, since electron-emissions are discrete and qualified as rare, such events ought to follow a Poisson law. Considering that the average number of electrons emitted per ion is fully determined by the yield curve  $\gamma(E)$ , the parameter of the chosen Poisson law must be  $\lambda(E) = \gamma(E)$ . To sum things up, each ion impinges on the cathode surface with an energy  $E$ . Depending on its value, the emission phenomenon will be either potential or kinetic. The average number of emitted electrons, for a large number of collisions with the electrode, at this fixed value  $E$ , will be  $\gamma(E)$ . Then, the probability for an ion with energy  $E$  to release  $k$  electrons, with  $k \in \mathbb{N}$  is

$$P(k) = \frac{e^{-\gamma(E)}}{k!}. \quad (10)$$

The cumulative distribution function corresponding to the PDF in Eq.(10) is then given by the following expression

$$C(k) = \sum_{j=0}^{\lfloor k \rfloor} \frac{\gamma(E)^j}{j!}. \quad (11)$$

Now that the probability for each event to occur is known, remains to implement the electron generator in the FENNECS code. To do so, a random number generator has been programmed such that the integers produced follow a Poisson law specified by  $\lambda := \gamma(E)$ . In order to achieve this generation, random numbers are generated uniformly in  $[0, 1[$ . Since the cumulative distribution function (CDF) of the probability law ranges in  $[0, 1[$ , the distance from these numbers to the pre-images of the CDF is evaluated. Then,  $k$  taken as the integer such that its image by  $C$  is immediately lower than  $r$ . Mathematically, this reads as follows:

- i) Generate a random number  $r$  uniformly in  $[0, 1[$ .
- ii) Evaluate the CDF of the law with  $\lambda = \gamma(E)$  as in Eq.(11).
- iii) If  $r \in [C(\tilde{k}), C(\tilde{k} + 1)]$ ,  $k = \tilde{k}$ .

In order to make sure that this way of generating random number according to the CDF in Eq.(10) is correct, a statistical survey over a large number of tests is ran, with several values for  $\lambda = \gamma(E)$ , and the obtained number of counts for each value of  $k$  is represented in Fig.(9). As expected for  $\lambda = 1$ , the number of counts for  $k = 0$  and  $k = 1$  are equal. Results show good agreements with theory for other values of  $\lambda$ , ensuring then that our Poisson random generator works fine.

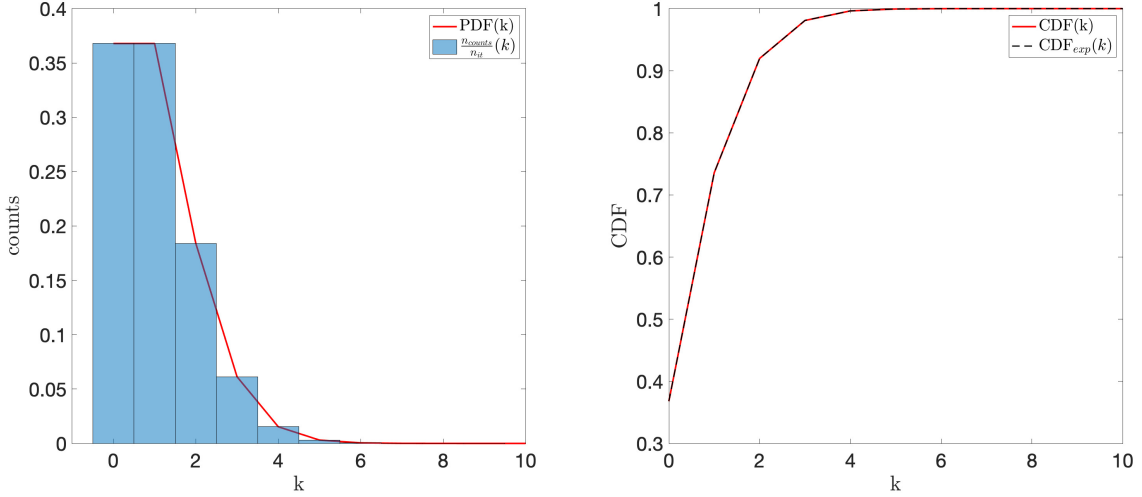


FIG. 9. Left: Normalised histogram for the number of counts obtained for each  $k$  following the Poisson law of parameter  $\lambda = 1$  with the expected  $P(k)$  (red) - Right:  $C_{\text{exp}}(k)$  obtained by summing the contributions from each bin of the histogram and  $C(k)$  the theoretical cumulative distribution function for  $\lambda = 1$ .

One more thing that had to be treated is the energy distribution of the emitted electrons. Indeed, all the electrons are not generated with zero velocity. The emission direction can also vary, but this will not be implemented. Regarding the energy distribution, according to [DH, PPZ<sup>+</sup>16], it seems that the emitted electrons' energy follows a gamma law, such that it averages at 2 eV. Recall that the gamma distribution varies in shape and in peak localisation according two parameters  $\kappa$  and  $\theta$ , with  $\kappa$  the shape parameter and  $\theta$  the scale parameter. Recall too that the mean is given by  $m = \kappa\theta$ .

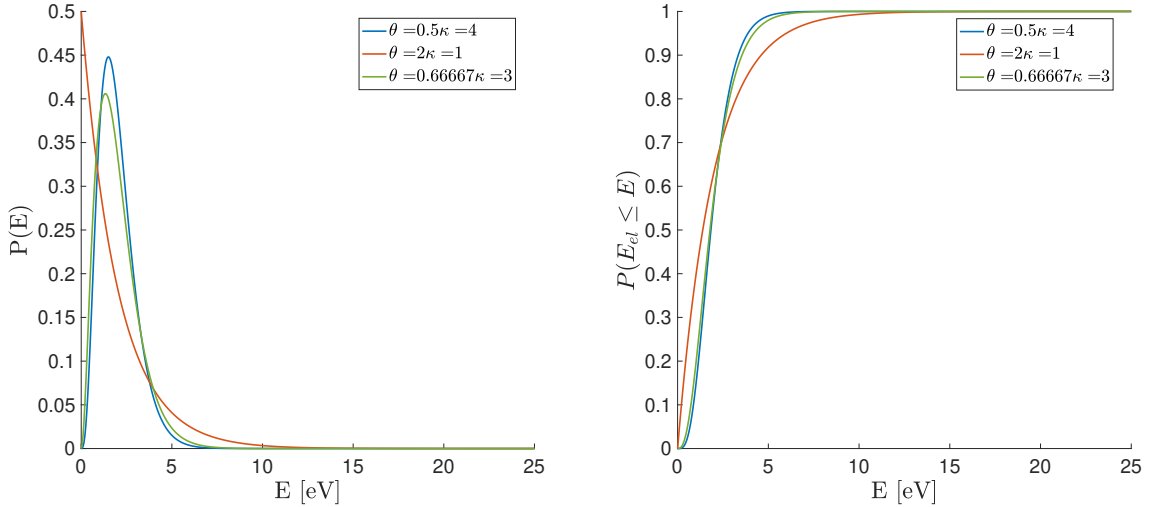


FIG. 10. Left: Gamma PDF for several  $(\kappa, \theta)$  couples - Right: Corresponding CDF.

Fig.(10) shows several gamma distributions with different couples  $(\kappa, \theta)$  such that  $m = 2$  eV. The couple that has been kept is  $(\kappa, \theta) = (0.5, 4)$ , so the peak probability would be closer to 2 eV. Recall that the probability density function and the cumulative distribution for a gamma distribution have the following forms:

$$P(E) = \frac{1}{\Gamma(\kappa)\theta^\kappa} E^{\kappa-1} e^{-\frac{E}{\theta}}, \quad (12)$$

$$C(E) = \frac{1}{\Gamma(\kappa)} \gamma\left(\kappa, \frac{E}{\theta}\right), \quad (13)$$

where  $\gamma\left(\kappa, \frac{E}{\theta}\right)$  is the lower incomplete gamma function.

Regarding the numerical implementation of the electron energy distribution in the FENNECS code, the same procedure as to produce a random number of electrons was applied, but in that case, the random numbers generated would not be integer anymore, and would follow a gamma distribution instead of Poisson. The difference in the number generation lies mostly in the discretisation of the range of values that could be taken. For Poisson generated numbers, only integer values can be taken, and hence, the construction conducted previously led to exactly Poisson distributed values. In the case of the electrons' energy, the latter can physically vary on a continuum. Our energy-values generator is hence limited by the degree of precision in the discretisation of the energy range. However, for our purpose, that is of a qualitative survey of the influence of ion-induced electrons, such precision is not required, since according to the large electric field values, no significant effect of the initial electrons' energy is to be expected. The random generation steps are listed below.

- i) Generate a random number  $r$  uniformly in  $[0, 1[$ .
- ii) Evaluate the CDF of the law with  $(\kappa, \theta) = (0.5, 4)$  in the range  $[0, 15]$  eV with  $N = 500$  points.
- iii) Take  $E$  as  $E := \min_{\tilde{E}} |r - C(\tilde{E})|$ .

Fig.(11) shows that our gamma random-number generator functions correctly. Indeed, following the same procedure as to statistically test the Poisson generator, one sees that over a large number of counts, the obtained distribution matches the gamma PDF.

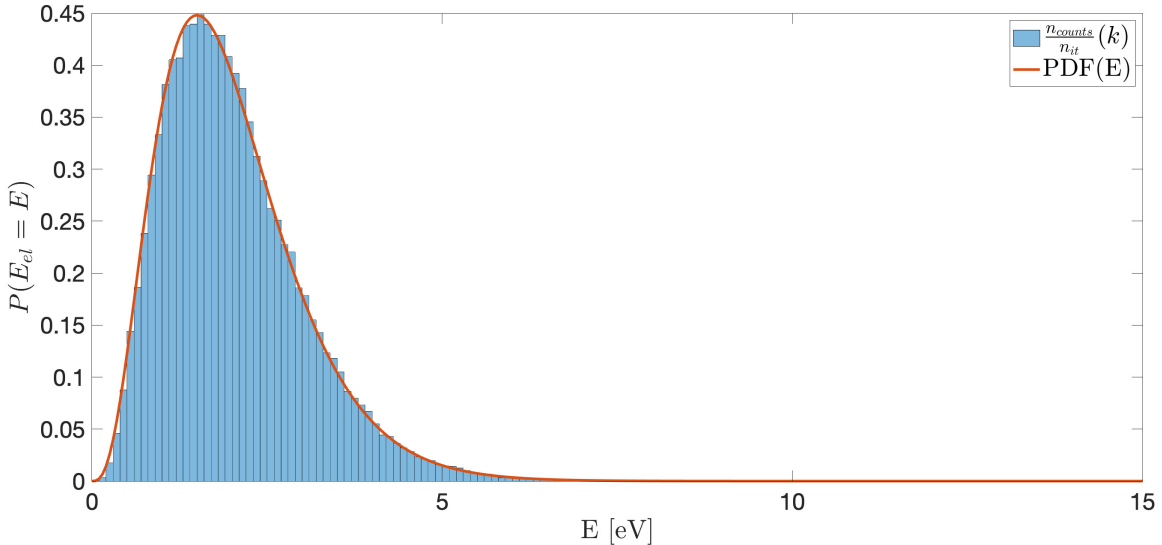


FIG. 11. Statistical results obtained from our gamma random-number generator. The red curve represents the analytical probability density function for this particular gamma distribution.

To put the module functioning in a nutshell, the process of generating electrons out of the ions loss consisted simply in combining the previous steps each time an ion was to hit the cathode. The full numerical treatment consisted in

identifying the ions that would hit the cathode and apply the external module taking account for electron emissions. Summing up the steps, each ion that disappeared would be identified evaluating the geometric weight [LB22], which would state that the particle is no longer in the simulation domain. Then, its energy would be evaluated, so that the average yield  $\gamma(E)$  would serve in generating a random number of electrons, for which some additional memory would have been allocated. These electrons would then be placed initially at the last position *inside* the domain, and be given an energy randomly generated according to the gamma law from above. The ion could then safely be removed from the particles, and the electrons would contribute to the newly updated population of particles. In light of that, it is important that the time step is short enough so the last recorded ion positions before they get removed, are close enough to the electrode, to avoid any spread effect as in Fig.(6). However, since the electrons are to be tracked to evaluate their potential contribution to any electron cloud, the time step should be already little enough. Fig.(12) illustrates the numerical treatment of cathode colliding ions.

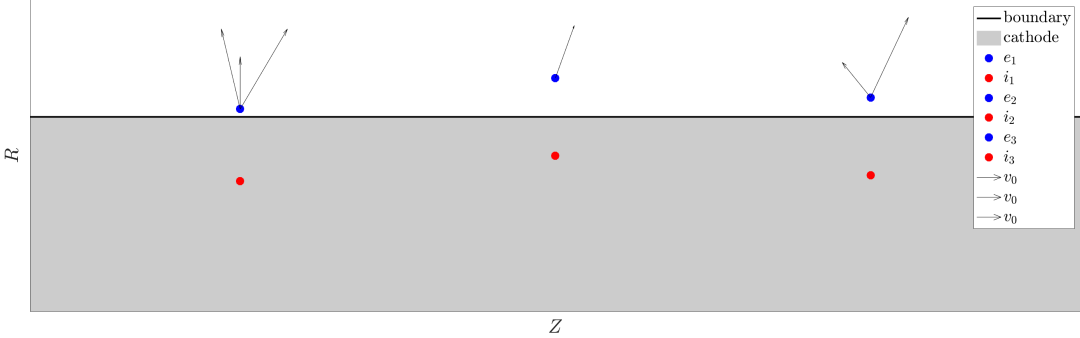


FIG. 12. Schematics of the situation where several ions are collected at the cathode, and a group of electrons is produced each time. Note that the number of electrons per incident ion is different, and the initial velocity vectors have different lengths due to the initial energy distribution

### III. RESULTS

#### A. Code testing

The IIEE module being implemented, some tests were required in order to check that the code behaves accordingly. To do so, several tests were realised. The first one consisted of statistical results for the yield. To derive a statistics, the simple geometry from Fig.(5) was implemented, as well as several horizontal slices of ions. These ions were initialised at different radial distances from the cathode. Making use of Eq.(2), their energy as they hit the electrode is known, and so is the average yield per incident ion. Recall that the yield is a function of the incident ion energy only, through the energy loss in the material,

$$\gamma(E) = \Lambda_{exp} \cdot \frac{dE}{dx} \Big|_i . \quad (14)$$

It is also important to note that the energy loss tables used to implement the yield curves as in Fig.(7) contained values for protons impinging on different materials. In order to obtain results exploitable for the TREX experiment, the yield for incident protons had to be replaced by the yield for other ions, as  $H_2^+$  for example. Approximatively, since  $H_2$  is a diatomic molecule formed of hydrogen atoms, which are protons when ionised, one can deduce the yield for  $H_2^+$  cations through  $dE(\tilde{E})/dx|_{H_2^+} \sim 2dE(\tilde{E}/2)/dx|_{H^+}$  [DH]. Hence, Eq.(14) reads

$$\gamma_{H_2^+}(\tilde{E}) = \Lambda_{exp} \cdot \frac{dE(\tilde{E})}{dx} \Big|_{H_2^+} = 2\Lambda_{exp} \cdot \frac{dE(\tilde{E}/2)}{dx} \Big|_{H^+} , \quad (15)$$

and then

$$\gamma_{H_2^+}(E) \simeq 2 \cdot \gamma_{H^+}(E/2). \quad (16)$$

For all three materials, the slices of ions were initialised along the axial direction, thus enabling to show that the electron generation from the code, over the loss of ions, is independent of the axial position, as expected. Fig.(13) shows the results for  $H_2^+$  cations impinging on the cathode made either of  $^{304}\text{SS}$ , Cu or Al. The potential bias applied between the two electrodes is  $\Delta\phi = 20$  kV. The magnetic field is uniform, with field lines parallel to the electrodes, and  $B = 0.21$  T, as it is a value of the order of magnitude used in gyrotrons. The radial positions of the electrode were  $r_a = 0.001$  m for the cathode and  $r_b = 0.01$  m for the anode, and the ions were generated at  $r_1 = 0.003$  m,  $r_2 = 0.005$  m and  $r_3 = 0.008$  m. Using the very simple equation Eq.(16), the expected yield could be estimated and the comparison of the latter with the one obtained from the IIEE module is exposed in Table.(I).

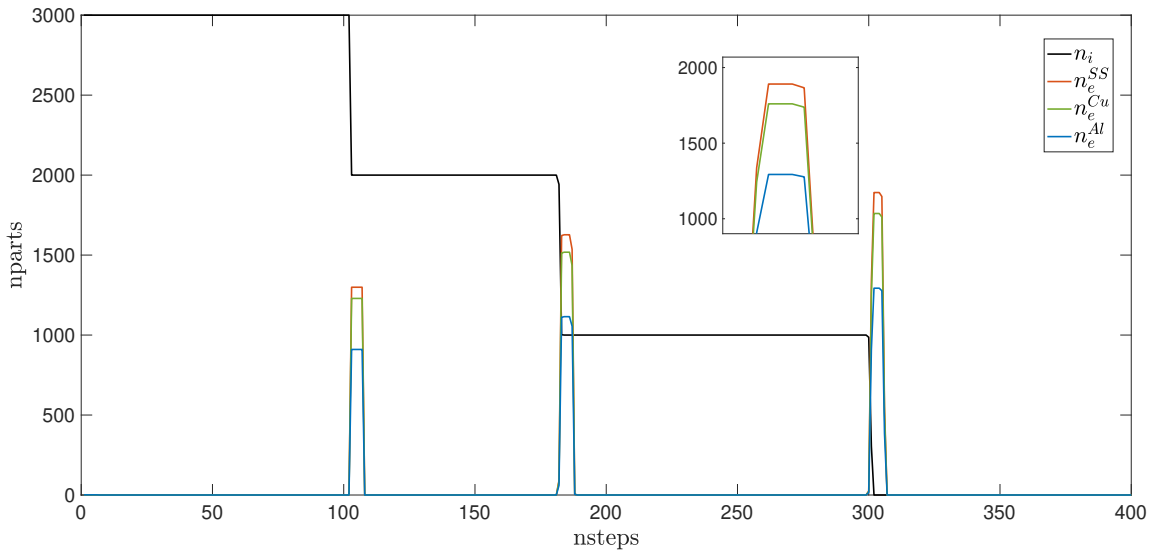


FIG. 13. Plot of the number of particles over the number of simulation time-steps. The black curve represents the number of ions, while the colored curves show the number of electrons produced in the impingement of  $H_2^+$  ions over  $^{304}\text{SS}$ , Cu and Al.

One notes on Fig.(13) that the ions population curve is discontinuous. It is due to the fact that the ions are initially configured in three slices at distinct radii, as shown in Fig.(14), and together with the symmetry of the system, they reach the cathode and disappear at distinct discrete times, hence the steps. Regarding the peaked shape of the electronic population curves, they disappear few time after being generated because in this geometry, the magnetic field lines are parallel to the electrodes. Thus, after a Larmor gyration, the electrons are not moving away from the cathode, and hence, they are recaptured few after being emitted.

The statistical results presented in Table.(I) are interesting in the sense that the theoretical model seems to have been implemented correctly. Regarding the relative errors, they are always lesser or equal to 1.6%, which is an acceptable value considering the fact that the model is approximative in several ways. Indeed, the yield conversion from  $H^+$  to  $H_2^+$  exposed in Eq.(16) is an approximation. The fact that the yield in the potential emission region was constant (see Eq.(7)), and that we linearly interpolated this constant value to the bottom of the kinetic emission model, constitutes one more source of approximation. However, this description is sufficient for a simple estimate of the influence of IIEE on electron clouds formation and behavior. Indeed, the yield being of the order of  $\sim 1 - 2$ , the approximations made should not influence or disturb greatly the expected results, in terms of electronic densities for example.

The last phase of the module testing was to determine whether or not some of the electrons generated by ions colliding with the electrodes would be kept in the simulation domain, or if no matter the geometry, they would be lost, as on Fig.(13). To do so, an initial non-zero ion density was implemented in a region that was known to trap electrons, in a geometry where the cathode has half an ellipse dug inside it, as shown in Fig.(15) - Left. This is one of the geometry planned to be mounted in the TREX experiment. No electron cloud was present at the time, so the potential well naturally present due to the topology of the  $\mathbf{E}$  and  $\mathbf{B}$  fields was not affected by the presence of an

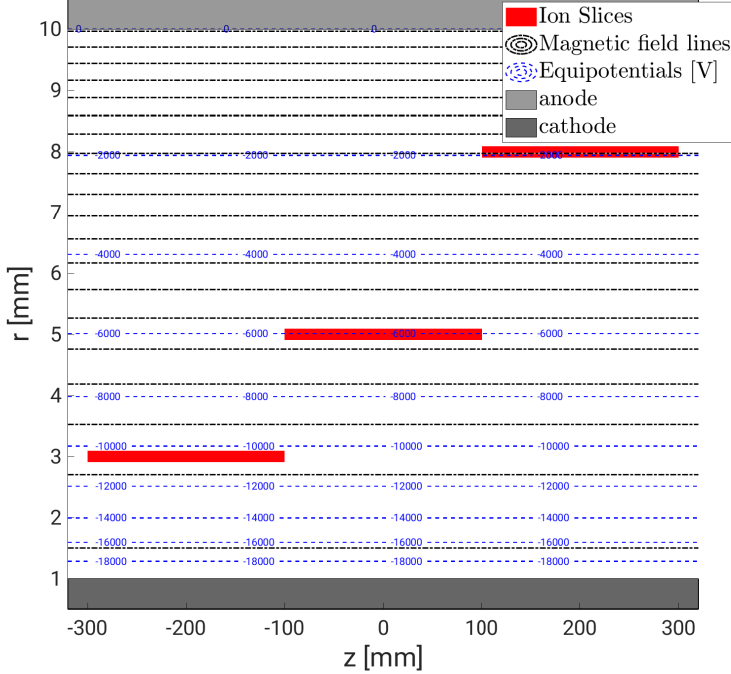


FIG. 14. Initial ionic configuration used to produce the statistics from Table.(I). The red stripes denote the initial ions positions. Note that by azimuthal symmetry, the ions are disposed on annuli.

	$E_1$	$E_2$	$E_3$
<b><math>^{304}\text{SS}</math></b>			
$\gamma_{th}$	1.311	1.623	1.870
$\gamma_{iiee}$	1.299	1.627	1.891
$\epsilon_{rel}$	0.9%	0.2%	1.1%
	$E_1$	$E_2$	$E_3$
<b>Cu</b>			
$\gamma_{th}$	1.237	1.522	1.746
$\gamma_{iiee}$	1.229	1.518	1.760
$\epsilon_{rel}$	0.6%	0.3%	0.8%
	$E_1$	$E_2$	$E_3$
<b>A1</b>			
$\gamma_{th}$	0.920	1.133	1.297
$\gamma_{iiee}$	0.910	1.115	1.293
$\epsilon_{rel}$	1.0%	1.6%	0.3%

TABLE I. Yield statistics for  $\text{H}_2^+$  ions impinging on the three materials

electron cloud. All the electrons produced at the electrode by IIEE were tracked down in a specific species in the code, so they would not be mixed up with the other electrons, coming from ionisations of the RNG. The right plot of Fig.(15) shows the orbits of two among all the electrons that have not left the simulation domain. One notes that they were trapped in the potential well, bouncing at its axial limits, while they were drifting azimuthally over several full poloidal periods. The radial width of the orbit is defined by the Larmor radius. With this information in hand, it appears that ion induced electron emissions could produce interesting results regarding the formation of clouds. For example, the formation time could be influenced, the maximum density too. This will be treated in the next subsection.

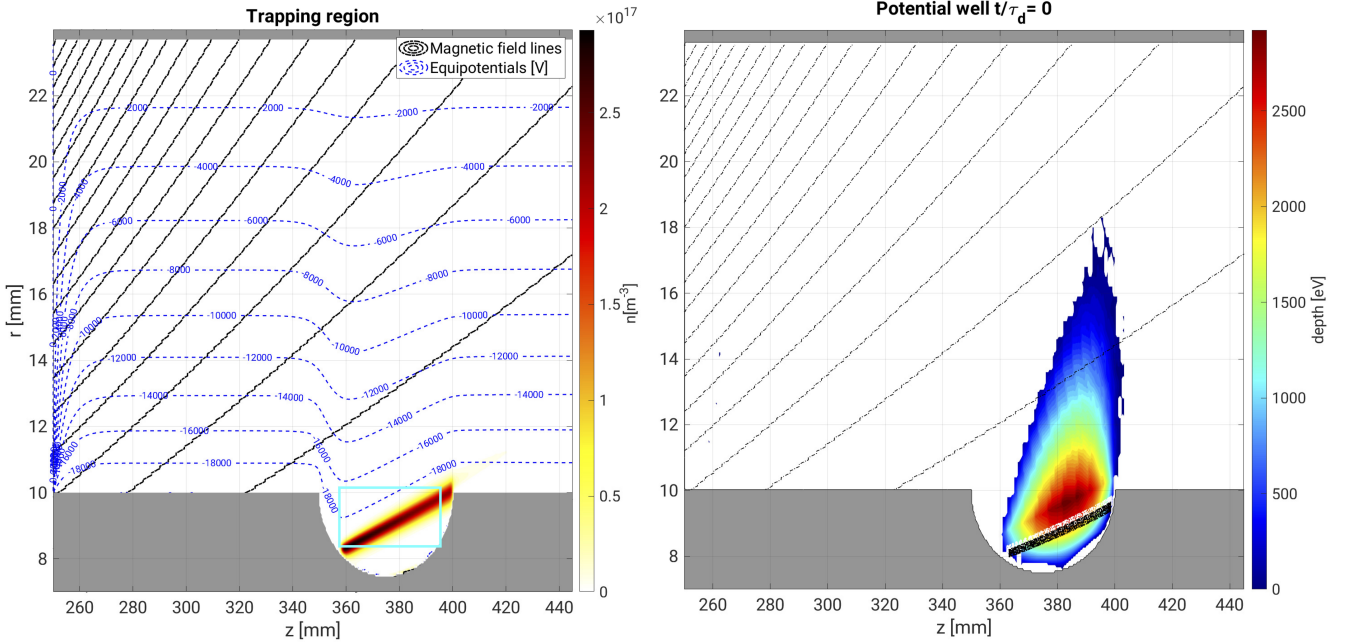


FIG. 15. Left: trapping region from the TREX extrude geometry. A cloud is present and the initial ion distribution is emphasized by the blue rectangle. - Right: vacuum potential well and two trapped electrons orbits.

### B. Cloud formation

Now, let us deal with results concerning the clouds formation and dynamic, with and without taking account for IIEE, and for Al electrodes. In first considerations, two particular TREX geometries have been implemented. Let us start with results in the *slanted* geometry, that is with a prominent half-ellipse coming out of the anode, as in Fig.(4).

#### TREX *slanted* geometry

Several characteristics are of interest in this case. As mentioned before, the characteristic time of cloud formation might be affected by the IIEE. The peak cloud density could also be increased. It can be interesting to look up the currents present at the boundaries too. Indeed, the stronger the electric current, the higher the risk for the power supply to fail at sustaining the potential bias. To obtain these informations, two situations are considered. The geometry is the same for both, that is with the ellipse protruding from the anode. The anode is grounded, and the cathode is at  $\Phi = -20$  kV. The magnetic field intensity is of about  $B = 1.15$  T on the high field side (low  $z$ ), and decreases down to  $B = 0.15$  T on the low field side (high  $z$ ). The neutral pressure is numerically set to  $2 \cdot 10^{-2}$  mbar so the formation time of the cloud is reduced. Hence, the results will be normalised by the collision time. The magnetic field topology and the initial electronic configuration are shown together in Fig.(16). Since the bottom of the ellipse is known to be a trapping region, a rectangle distribution of electrons is initialised below it, in order to act as a source of ionisation, to produce the ions by collisions with the RNG. Now two cases are to be distinguished: the case with and the case without IIEE.

Let us first compare how fast the steady state is reached in both situations. Recall that the steady-state is characterized by the ions loss equal to the electrons loss. Hence, this is supposed to imply that the ionic current and the electronic current are constant over time, and of the same order of magnitude. Regarding the number of particles, it is supposed to reach a maximum and stagnate more or less, before decreasing in absence of a source to sustain the cloud filling. The time required to reach this maximum corresponds to the cloud formation time. Plotting the total electronic charge over time can be a great indicator of the state of formation of the cloud. It can also enable to compare the formation in the two situations, where IIEE are considered and not.

On the left part of Fig.(17), the absolute value of the total electronic charge in the domain is represented over time, the time being normalised by the collision time, to remove the pressure dependency. The blue curve represents

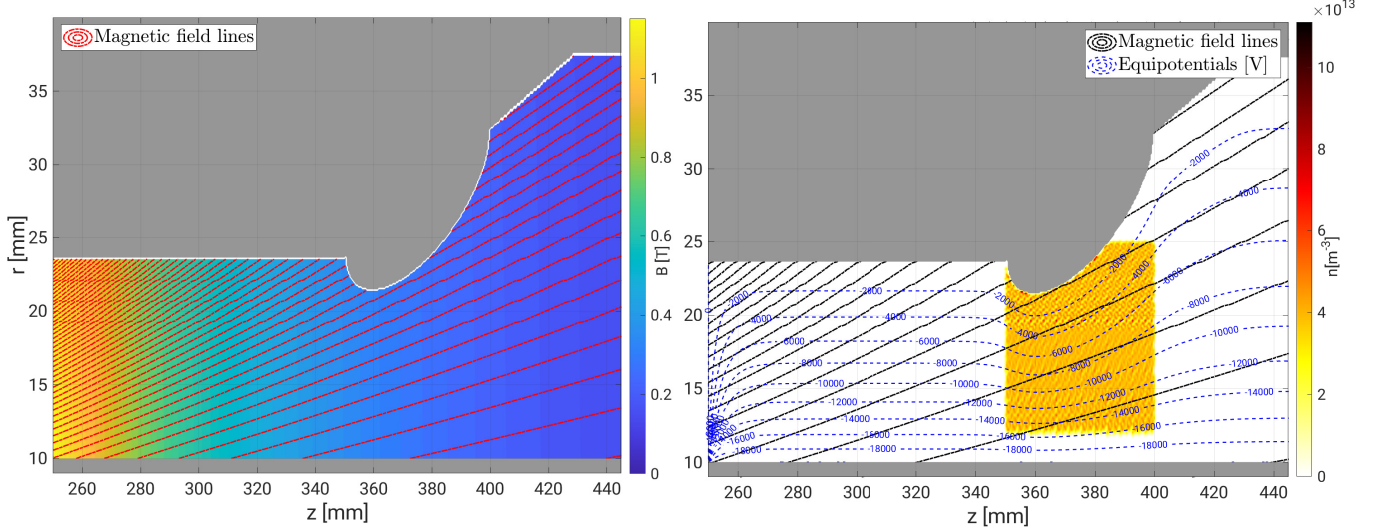


FIG. 16. Left: magnetic configuration from the TREX slanted geometry. - Right: initial configuration of electrons, leading to the formation of an electron cloud.

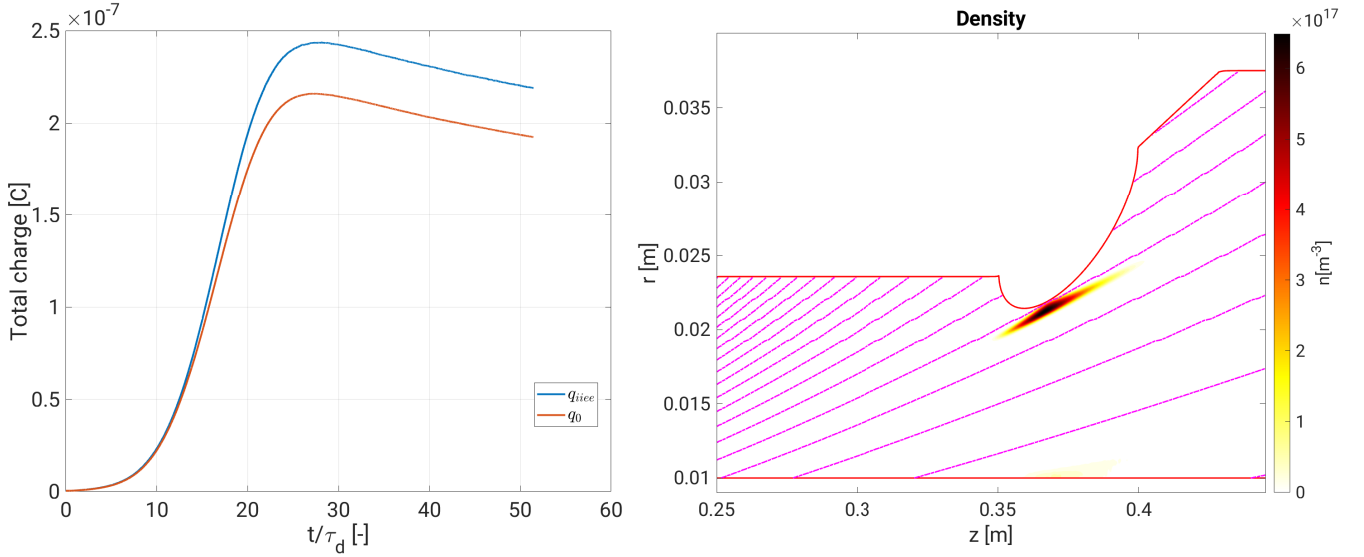


FIG. 17. Left: evolution of the total electronic charge inside the domain, over time normalised by the collision time. The difference in charge is due to the electrons generated at the cathode, under the cloud. - Right: electron density in steady state.

the charge when the ion induced emissions are taken into account. One notes that the formation times are similar, since the inflexion point of each curve is located at about the same time, and so is the peak value. As expected the charge is higher, since more electrons have been produced. Note that this information alone is not sufficient to determine whether the total charge is higher because more electrons have accumulated in the cloud, or if they are present elsewhere in the domain. This is why the electron density is plotted in steady state, on the right plot of Fig.(17). Although it is not represented, both clouds, with and without IIEE had the exact same density and shape (hence, for the sake of saving space, only the situation with IIEE has been shown). This is consistent with our expectation, since the ion-induced electrons are formed at the cathode, and the potential well is located right by the anode. It is clear that these electrons, due to their Larmor motion along field lines, cannot reach the cloud and be trapped too. They will simply leave the domain axially, and contribute to a source of axial current. Now, one question arises: what is the order of magnitude of this ion-induced electronic current ?

To answer this question, the currents collected at all the boundaries of the domain have been plotted over time. The boundaries are the axial limits,  $z = 250$  mm and  $z = 445$  mm, and the metallic electrodes. The curves shown in Fig.(18) corresponds to the currents collected in the case where the IIEE were not considered. The purple curve corresponds to the electronic current collected in the region of the ellipse, as the cloud is progressively compressing against the electrode and leaking electrons towards the metal. The plain green line corresponds to the electronic current at the cathode, which is consistently approximately zero. The green dashed line corresponds to the ionic current at the anode, while the yellow plain line shows the axial current at the low field side, that is electrons leaking from the potential well as it is progressively squeezed against the anode (see Fig.(20) for the evolution of the potential well). The black plain curve represents the total current, that is the sum of all these contributions. The dashed black curve corresponds to the sum of all currents from Fig.(19), for the sake of comparison. The blue (plain) line shows the evolution of the electron density  $n_e$  over time, in order to visualise when the steady state is reached, while the dashed one corresponds to the electrons density in the lower radial half of the domain. Note that the time has been normalised here by the collision time  $\tau_d$ . As predicted, in steady state, the ionic (dashed green) and electronic (purple + yellow) are constant and of the same order. Of course, no current is collected on the high field side.

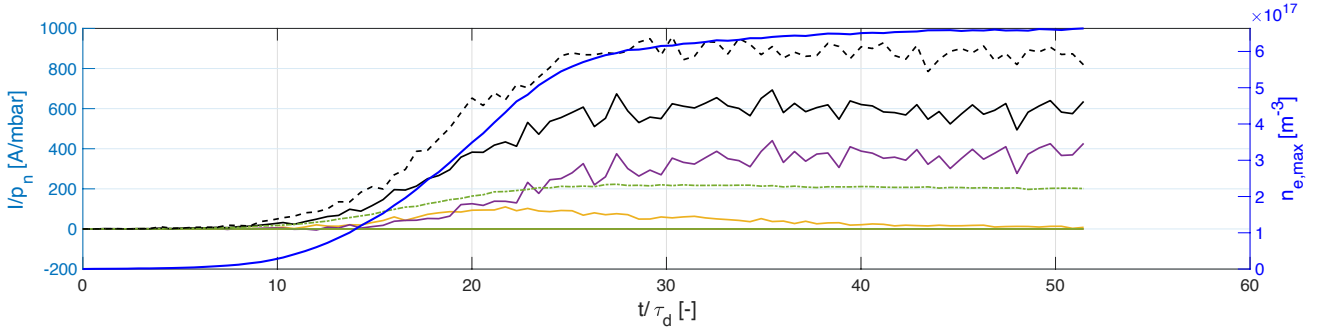


FIG. 18. Currents collected at all the boundaries of the domain, in absence of ion induced electron emissions. The colors correspond to the domains highlighted at the bottom part of Fig.(19)

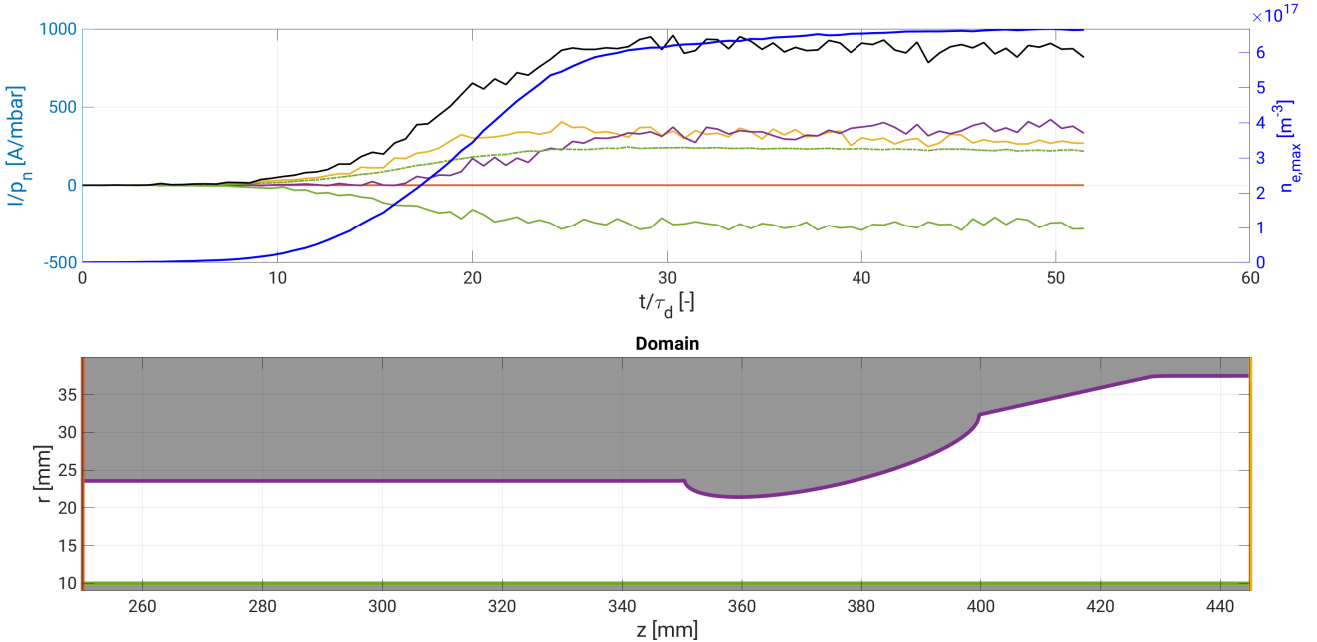


FIG. 19. Top: Currents collected at all boundaries of the domain, taking account for IIEE. - Bottom: Domain and boundaries definitions. The high field side is in red on the left, the low field side in yellow, the cathode in green and the anode in purple.

The high plot from Fig.(19) represents the same information as in Fig.(18), with the exact same color code. However, the contributions to the different currents might change a little bit. Still, no current is collected on the high field side. The electronic current collected at the anode is approximately the same in both situations, emphasising that the cloud behavior does not depend on IIEE in this geometry. However, now a contribution (negative) of the total current at the cathode is present (green, solid line). This contribution is due to the electrons leaving the cathode as they are produced by the ions. Note that since the yield is on average, of the order of 1-1.5, the ionic current (green dashed) is approximately equal and of opposite sign as the electronic current leaving the cathode. The generation of electrons at the electrode being discrete events, the currents fluctuates a bit more around its average value.

Since the ions and the electrons have opposite charges, and they flow in opposite directions, the negative current at the cathode, coming from the electrons, will contribute to a new net current towards the grounded region. Indeed, all electrons being generated at the cathode are flowing towards the low field size to leave the domain. Thus, it is expected that the axial current is at least as important as the electronic current induced by electrons leaving the cathode. It turns out that it is even greater, since it contains the contribution from the electrons that are leaking from the cloud, see yellow line on Fig.(18). The total current flowing from the cathode (at  $\Phi = -20$  kV) to the grounded regions (low field side and anode), plotted in black, is now greater of about 40 – 50% than the total current observed without ion induced emissions.

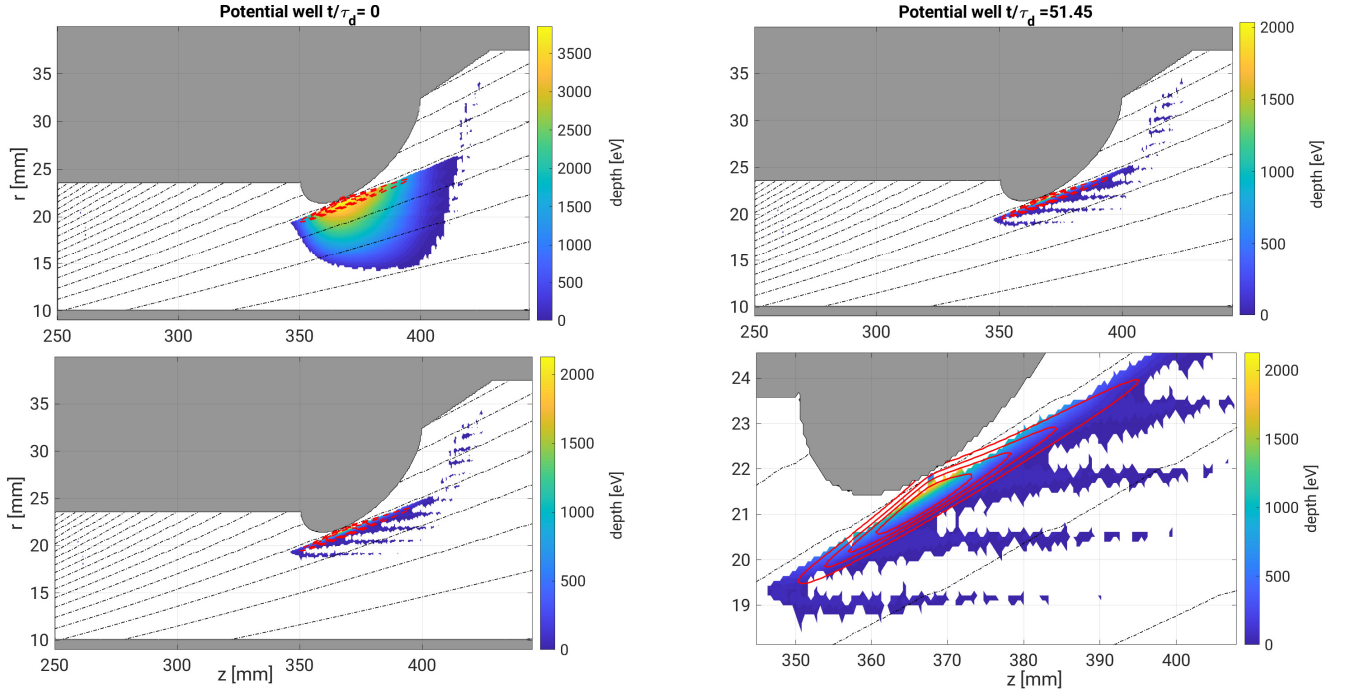


FIG. 20. Potential well dynamics as the electron cloud forms. Up Left: Vacuum potential well - Up Right: Potential well in presence of the cloud (IIEE) - Down Left: Potential well in presence of the cloud (without IIEE) - Down Right: Zoomed view

The dynamic of the potential well as the cloud is forming is shown in Fig.(20). The upper left corner plot shows the vacuum potential well, that is the well formed naturally by the magnetic field line crossing the equipotentials, in absence of the cloud. For the sake of readability, the equipotentials have not been shown. The dashed red contours show where the cloud forms inside the potential well. The upper right and lower left corners plots show the potential well in presence of the cloud, with IIEE and without them respectively. Note that the wells are identical, as expected from the previous considerations. The lower right corner plots shows a zoomed view of the potential well, with the contours out of the cloud. Note that the outer contour intersects the anode, explaining the purple curve in Fig.(18-19), since some electrons from the cloud are collected at the anode. The potential well depth is remarkably affected by the cloud (see colorbar).

So to sum things up, the IIEE in this particular geometry seem not to influence neither the cloud formation time, nor the density. The clouds behave the same both with and without the ion induced electrons. As said previously, this can be explained by the magnetic topology, preventing the electrons leaving the cathode to reach the cloud's

potential well. However, it is important to note that the electrons produced by the ions contribute to a non-negligible net current component, that adds up on top of the other contributions, coming from the cloud leaking electrons, and the ions. Hence, this new contribution might have to be taken into account in the dimensioning and the design of the power supply for the MIG.

### TREX extrude geometry

Now, let us focus on one of the other designed geometries for TREX, the so called *extrude* geometry, that is with half an ellipse dug inside the cathode. The electrode geometry has been shown previously in Fig.(21). Here again, the anode is grounded, and the cathode is set at the potential  $\Phi = -20$  kV. The neutral pressure is set at  $P_n = 1 \cdot 10^{-1}$  mbar. The magnetic field intensity is the same inside the domain, and designed to reproduce the field from a superconducting magnet outside the domain, on the high field side. In the region of the ellipse,  $B$  ranges  $\sim 0.22 - 0.35$  T. The vacuum potential well, as defined previously, is shown in the right plot of Fig.(21). This ellipse aims at reproducing the bottom part of the trapping region, under the corona ring from a typical MIG, as shown in the dashed red region from Fig.(2). It is also located in the same axial region as the outer ellipse from the *slanted* geometry studied above, in order to later combine the two geometries, to be closer to the full MIG shape. However, splitting the study in two makes it easier to identify the physical phenomena influencing the formation of the clouds, and to separate the currents components. Indeed, taking the geometry where both the inner and the outer ellipses are present would lead to two clouds, preventing us from determining easily which cloud is responsible for which current and so on. Nevertheless, this would be the object of an interesting further study.

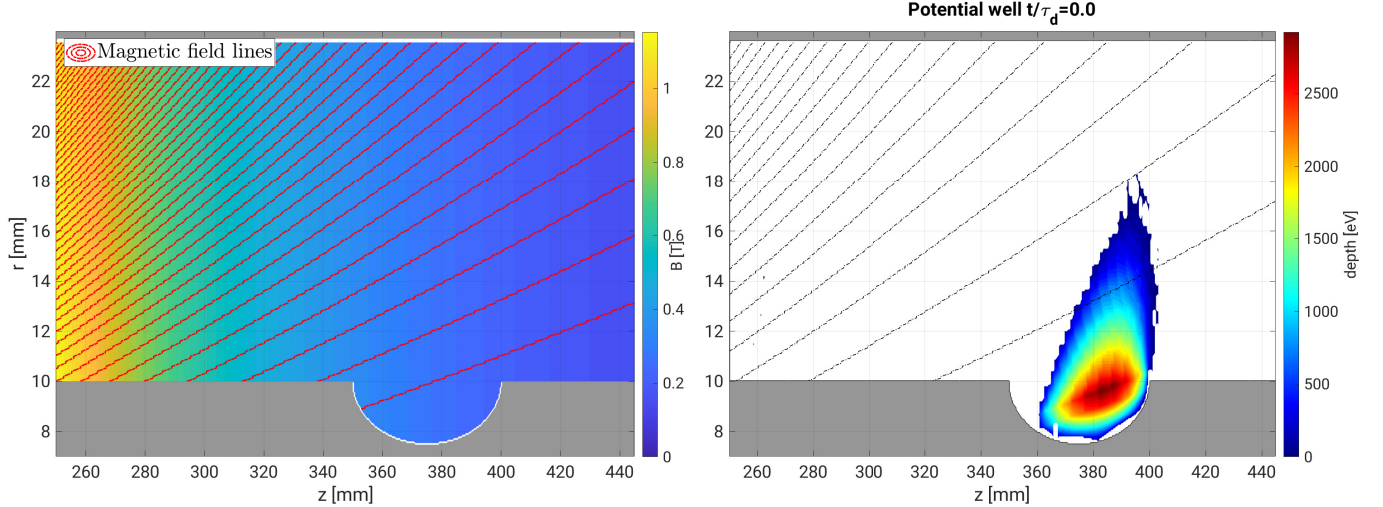


FIG. 21. Left: magnetic configuration for the extrude geometry. The high field side is on the left and the magnetic field lines are shown in red. - Right: Vacuum potential well in the same geometry.

In order to carry out the same kind of study as for the slanted configuration, several characteristics have been studied, the main goal being to compare electron clouds formation with and without IIEE, and how the electric currents collected at the boundaries of the domain are affected too. Let us first review the cloud formation times. It has been stated previously how the steady state is characterised, especially through the total charge evolution. The absolute value of the total electronic charge in the domain is plotted over normalised time, in the left plot of Fig.(22). The striking information is that here, contrarily to the case with the outer ellipse, the steady state is reached much faster. Indeed, the plateau is reached with IIEE about twice as fast as without.

The equilibrium state of the cloud without ion induced electrons is shown on the right plot from Fig.(22). To be able to compare the latter, the cloud in steady state with IIEE is shown in Fig.(23). Both the right and left plots are with IIEE, but different initial conditions. This will be discussed below. Coming back to the steady state cloud densities, with and without IIEE, they are of the same order, although the case with ion induced emissions shows a density greater of about  $5 \cdot 10^{16} \text{ m}^{-3}$ . Moreover, note that the cloud positions are different. The cloud formed in presence of ion induced emissions is located a bit lower inside the ellipse than without. This can be explained by the fact that a lot of electrons being generated at the cathode boundary, in the trapping region, the potential well tends to be

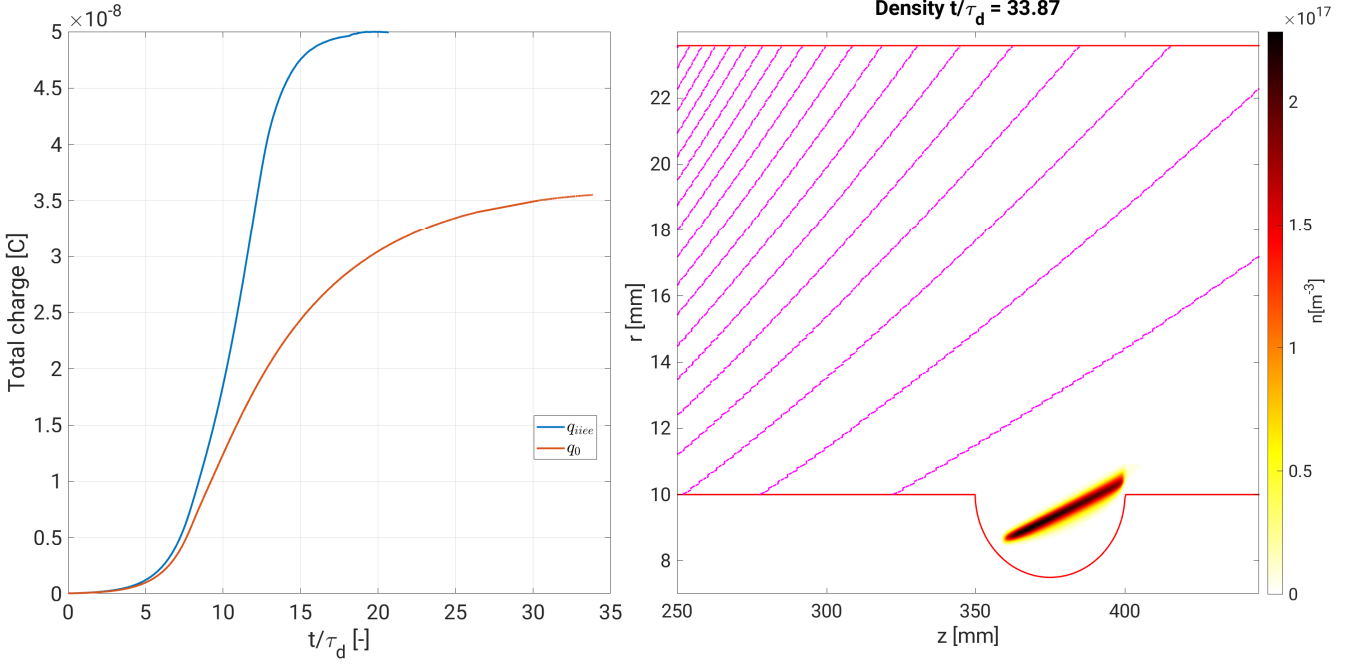


FIG. 22. Left: total (absolute) charge in the domain over normalised time. This time, the charge difference is due to the difference of cloud densities. - Right: Final state and cloud density in absence of ion induced electron emissions.

filled by the bottom. As the density grows inside the well, the latter becomes progressively narrower and its depth is decreasing as the potential is screened by the charge density (see Fig.(28) - Right). Without ion induced emissions (Fig.(28) - Right), the well tends to be filling by the top, since the electrons are being generated mostly in the ellipse region, not at the cathode surface. This explains the fact that the potential well remains deep in its bottom part, and hence the upper position of the cloud.

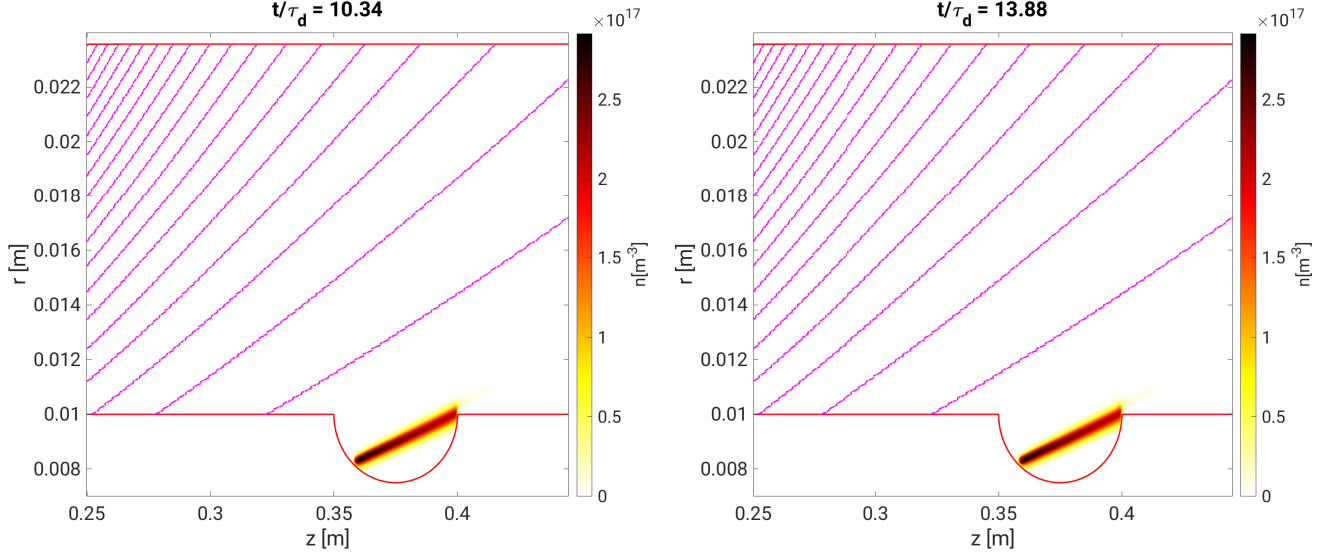


FIG. 23. Steady state electron clouds with ion induced electron emissions, corresponding respectively to the left and right initial electron distributions from Fig.(24).

The formation of this particular cloud is the result of a self sustained process arising from IIEE, since according to Fig.(23) and Fig.(24), different configurations can lead to this equilibrium. Indeed, the initial electrons and ions do not need to be generated in the region of trapping, inside the ellipse. However, due to the fact that the Larmor radius of the ions is of the order the meter (see Sec.(II C)), they travel almost in straight line towards the cathode, so they need to be formed above the ellipse for the induced electrons to be generated in the trapping region. In fact, if the ions were to be formed elsewhere, say in high field region, the electrons that would be induced at the cathode surface would just be lost at the low field side, after being guided along magnetic field lines. Note that the formation time is a variable of the initial electron distribution. Indeed, the more electrons and ions initially present in the ellipse region, the shorter the formation time. The times indicated in Fig.(23) correspond to the times when configuration reached the same peak density.

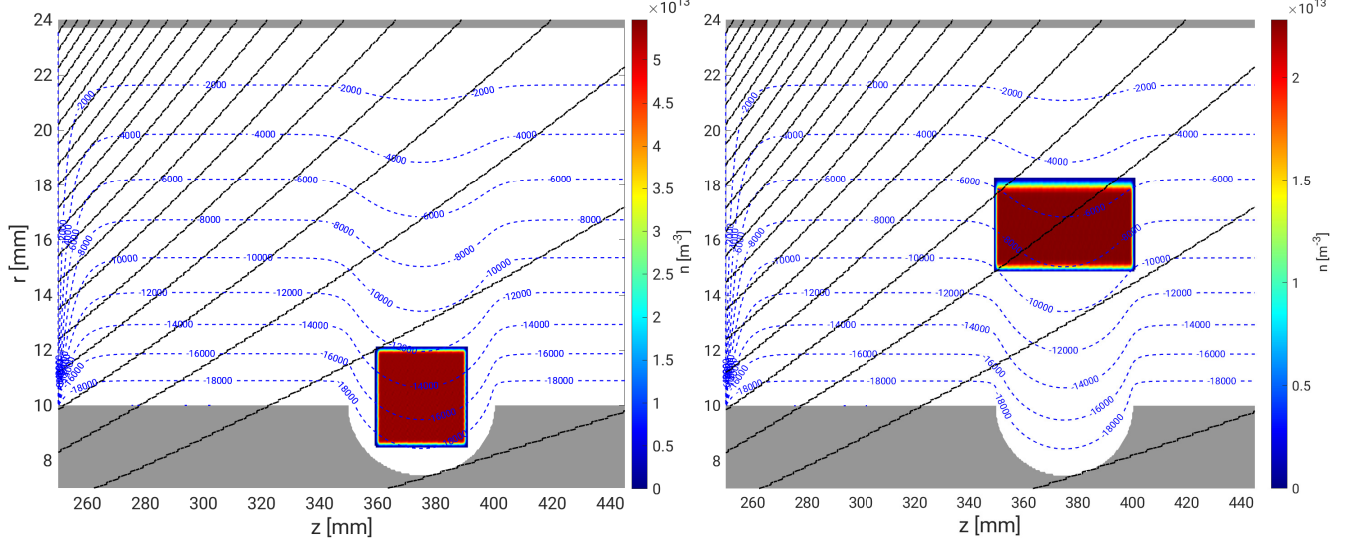


FIG. 24. Initial electron distributions leading to the clouds shown in Fig.(23), taking account for ion induced electron emissions.

The last part of this study in the extrude geometry is dedicated to the currents collected at the boundaries of the domain. Results are presented the exact same way as they were previously, in the slanted geometry. In absence of ion-induced electrons, the results are presented in Fig.(25). The dashed green line represents the currents from ions hitting the cathode. The yellow line is the axial current, measured on the low field side. Considering the radial position of the right tip of the cloud, this axial currents comes mainly from electrons leaking from the potential well (in steady state). Initially (left part of the curve), it is coming from the electrons that are lost as the initial distribution is colliding with the neutrals, producing more electrons. As the cloud grows, the electron population is densely localised in the trapping region, hence becoming the only source of axial current. The expected plateau is present in steady state. The total current flowing from the cathode to the grounded regions is shown in black. For comparison matters, the dashed black curve shows the evolution of the total current taking account for IIEE. The curve stops before the solid black one since as explained in the discussion around Fig.(22), the cloud steady state was reached much earlier. The electron density in the lower half of the radial domain is shown in solid blue. The dashed blue corresponds to the upper half.

The case with IIEE is depicted in Fig.(26). The domain boundaries are emphasised again with the color lines from the bottom plot. The contributions to the currents from each particle species can be identified having a look at Fig.(27). It shows the current densities at the electrodes and at the axial limits of the domain, in both cases, for electrons and ions. Note that this time, on Fig.(26), an electronic contribution to the current collected at the cathode is present. It comes from the electrons that are emitted inside the ellipse, and recapture at the electrode surface. Some of them are trapped in the cloud, and some others are guided towards the wall of the ellipse. This current vanishes in steady state. The ionic current (dashed green) and the axial current are slightly higher, resulting in a total current between the cathode and the ground to be higher too, of about 20 – 30%. The fact that the axial current is higher can be explained as follows: as the cloud is a little denser, more electrons are coming out, increasing the cloud contribution to the axial current. This is combined with the fact that the electrons that are leaving towards

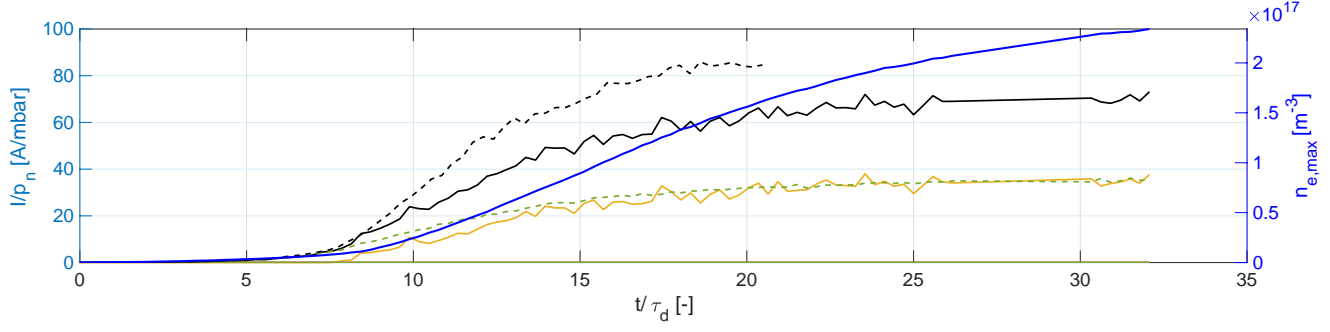


FIG. 25. Current collected at all the domain boundaries, without ion induced electron emissions. The color code is the same as the one used for the slanted geometry. The total current from Fig.(26) has been superimposed for the sake of comparison. However the curve is interrupted earlier since the steady state was reached much faster.

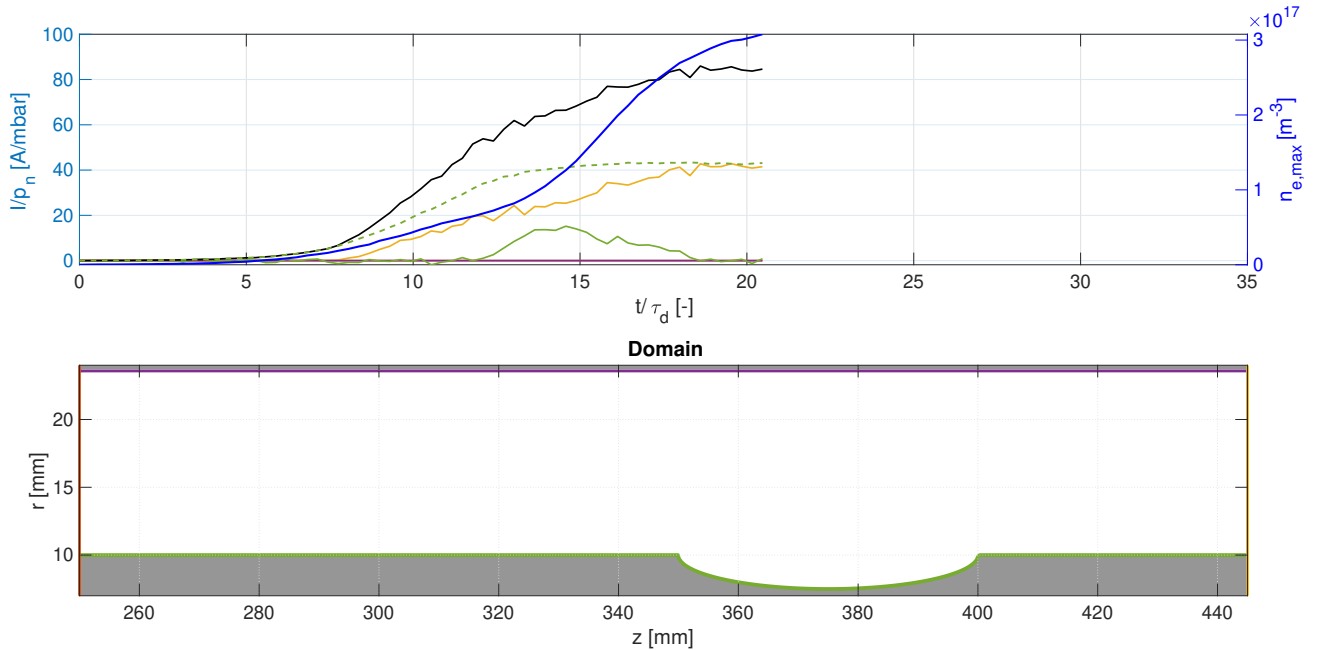


FIG. 26. Current collected at all the domain boundaries, with IIEE. The color of the curves matches the highlighted domain boundaries. The dashed green still represents the ionic current at the cathode.

the low field side produce ions by inelastic collisions on their way out. Since IIEE are considered, new electrons appear at the cathode surface, but in a region where no trapping can occur. They simply add to the existing electron flux in that area, increasing the axial current, and contribute in the formation of more ions too. Fig.(27) confirms that last information, since on right plots, the ionic current density is slightly higher in the ion-induced emissions case.

To draw a conclusion on this part, two of the TREX possible geometries were implemented, and results were shown in terms of cloud formation times, densities, and produced currents. In the *slanted* geometry, the cloud characteristics were not changed by ion-induced electron emissions, but the currents produced were, since some additional contributions were to be considered. The total current appeared significantly higher than in absence of IIEE. In the *extrude* geometry, the cloud was affected in the sense that the steady state was reached much faster with IIEE. The density was higher of about  $5 \cdot 10^{16} \text{ m}^{-3}$ , which corresponds to an increase of about 20%. Regarding the currents, the axial contribution was increased a little, hence so was the total current. If one were to consider the two geometries combined, as to reproduce the ITER GT-170 MIG, one would expect the currents flowing inside the MIG to be raised, and the density of the bottom cloud to be greater too. These might then influence the power supply, and create voltage stand-off problems.

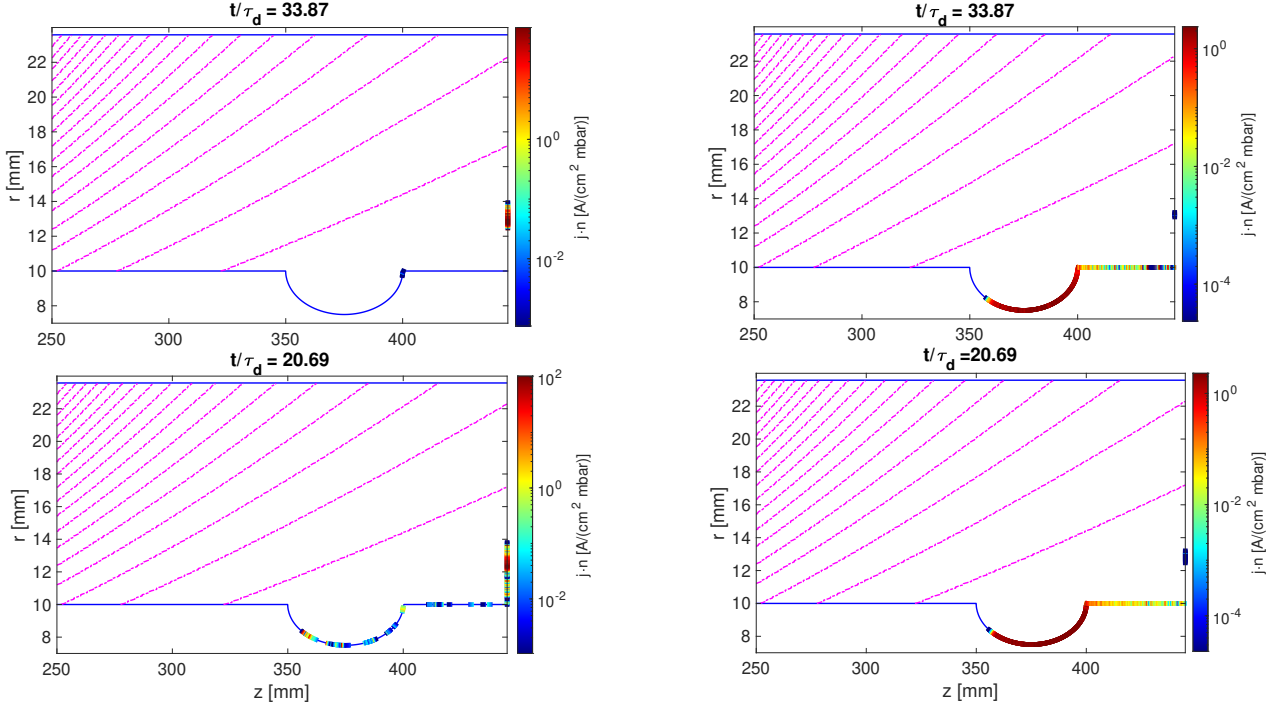


FIG. 27. Top: Current densities in steady state for electrons (left) and ions (right), without ion induced electrons. Bottom: same with IIEE.

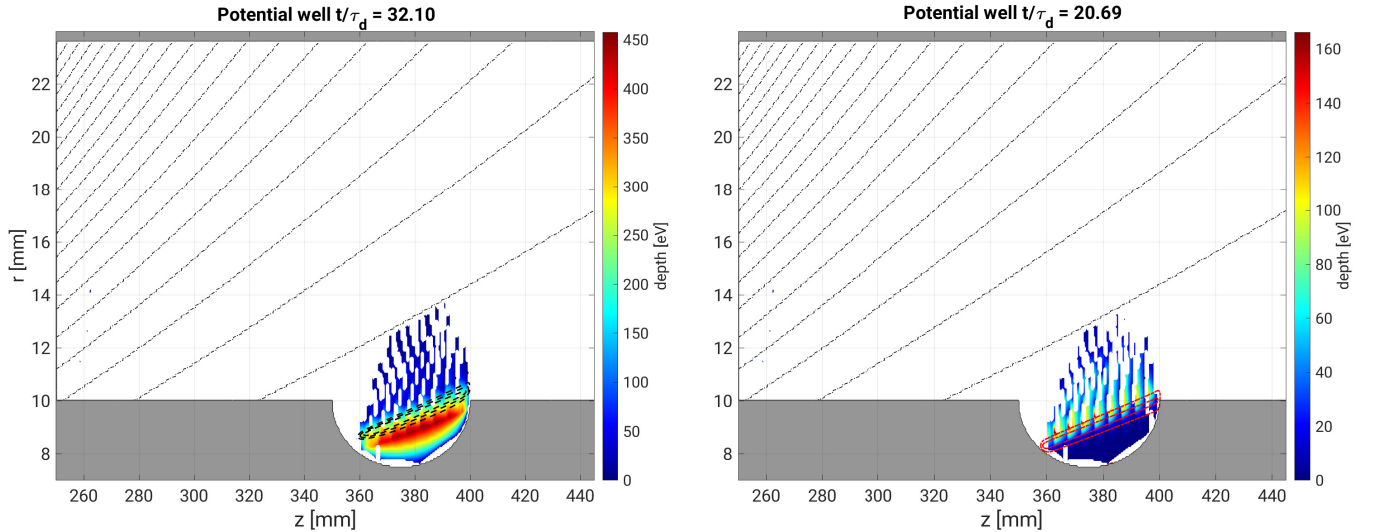


FIG. 28. Left: Potential well in presence of the cloud, in steady state, without ion induced emissions. Some cloud density contours are given in dashed black. The innermost contour has a greater density than the outermost. Right: Same, but with ion induced emissions. For readability purpose, the density contours are shown in red. The time has been normalised.

## ITER gt-170 refurbished MIG

Let us now focus on the previously introduced ITER GT-170 geometry. This MIG geometry is of interest since it is part of the gyrotrons that have been designed for ECRH for the ITER project [DAB<sup>+</sup>16]. The magnetic field intensity inside the MIG is defined as in Fig.(29) (left), and the equipotentials are such that two magnetic wells are present (see Fig.(30)). This is consistent with our expectations from the combination of the two geometries from TREX. The two potential wells have approximately the same depth. In order to study the formation of the two electron clouds in this geometry, an initial distribution of electrons has been implemented in the whole trapping region, as emphasised on Fig.(29) (right). The neutral pressure is set at  $P_n = 2 \cdot 10^{-2}$  mbar. The system is then left to evolve, with and without ion induced electrons. The expected results are a combination of what has been observed in the two previous sections.

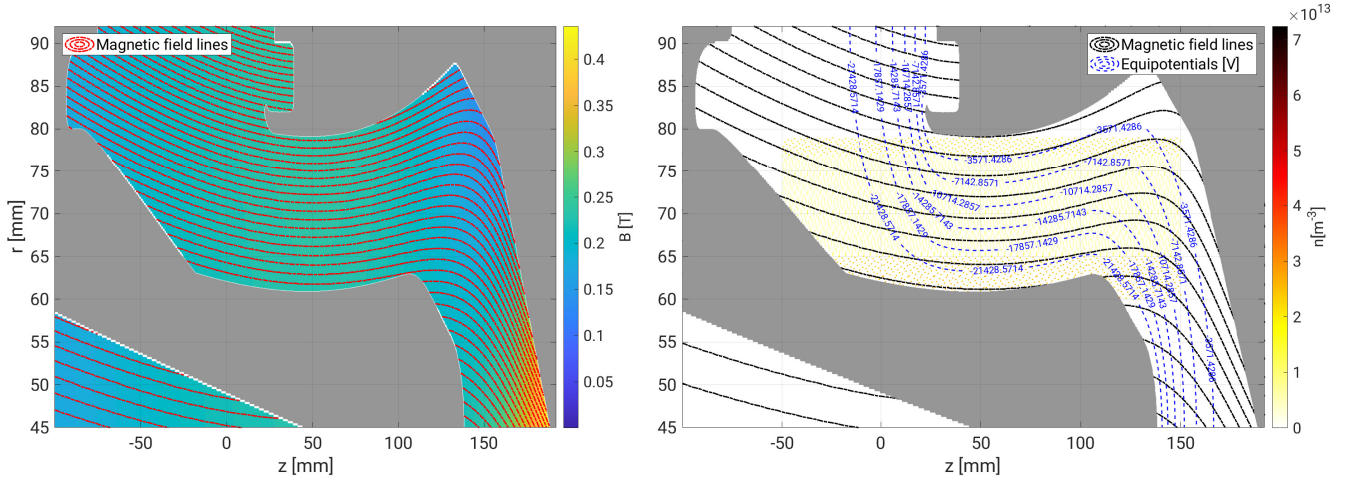


FIG. 29. Left: magnetic field intensity inside the MIG chamber. The magnetic field lines are plotted in red. - Right: Magnetic field lines (black) crossing equipotentials (blue), inducing two potential well shown in Fig.(30). The yellow dotted region corresponds to the initial electron distribution.

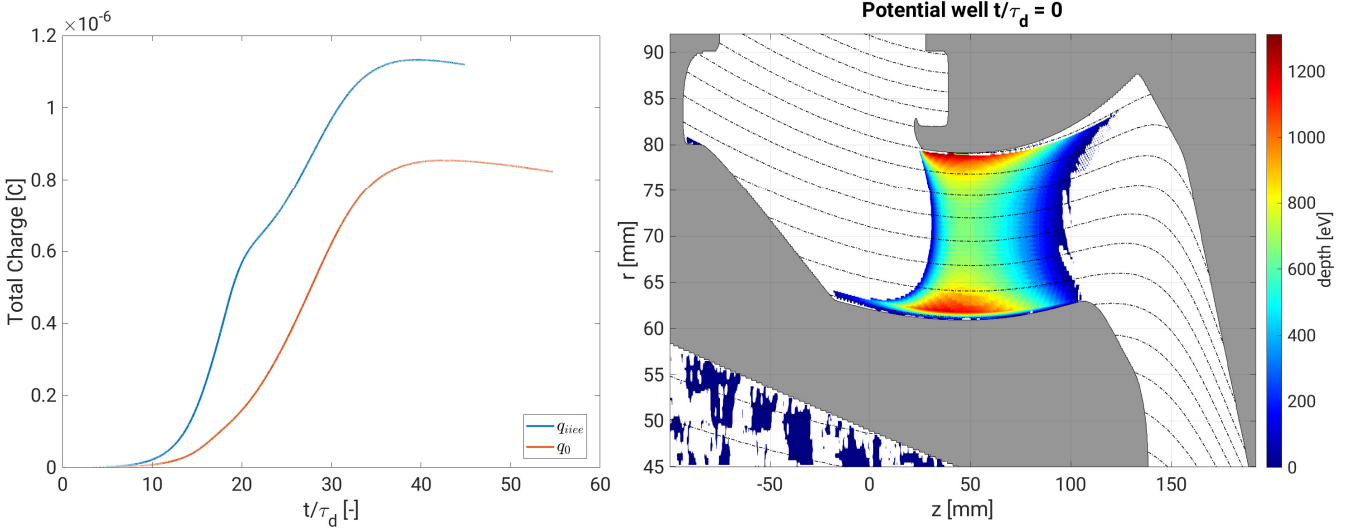


FIG. 30. Left: Evolution of the total charge inside the MIG chamber. The blue curve shows the case with ion-induced electrons. - Right: Potential wells present inside the MIG due to the magnetic and electric fields topology.

The total charge (of electrons) inside the domain over the normalised time is being shown in Fig.(30). The steady states are reached at similar times, although the case with IIEE got there a bit earlier. Without much surprise, the

total charge is higher for the case with IIEE. However, one notes that the growth rate of the charge in the domain is not continuous, as it slows down at the middle. This is due to the fact that the lower cloud filled faster the upper cloud, since the ion induced electrons were generated in its trapping region. The steady state was achieved when both clouds reached their maximum densities.

In order to show the influence of the electron clouds on the potential wells, the latter were represented in presence of the clouds, in steady state, in Fig.(31). The upper cloud contours are similar between the two plots, as predicted by our TREX simulations from the slanted configurations. This is great since it proves that the geometries used for the TREX experiment which is currently being built, enable to reproduce results from gyrotron guns such as this one. The lower cloud, as for it, is sensitive to the ion-induced electrons. Indeed, with IIEE, it is located lower than without. The potential well is more screened (see colorbar from Fig.(31) - left). Once again, this is a confirmation that the results predicted for TREX are consistent, when aiming at reproducing a gyrotron gun. Recall that we had observed the positions of the clouds in the ellipse to be different, one being slightly offset radially from the other.

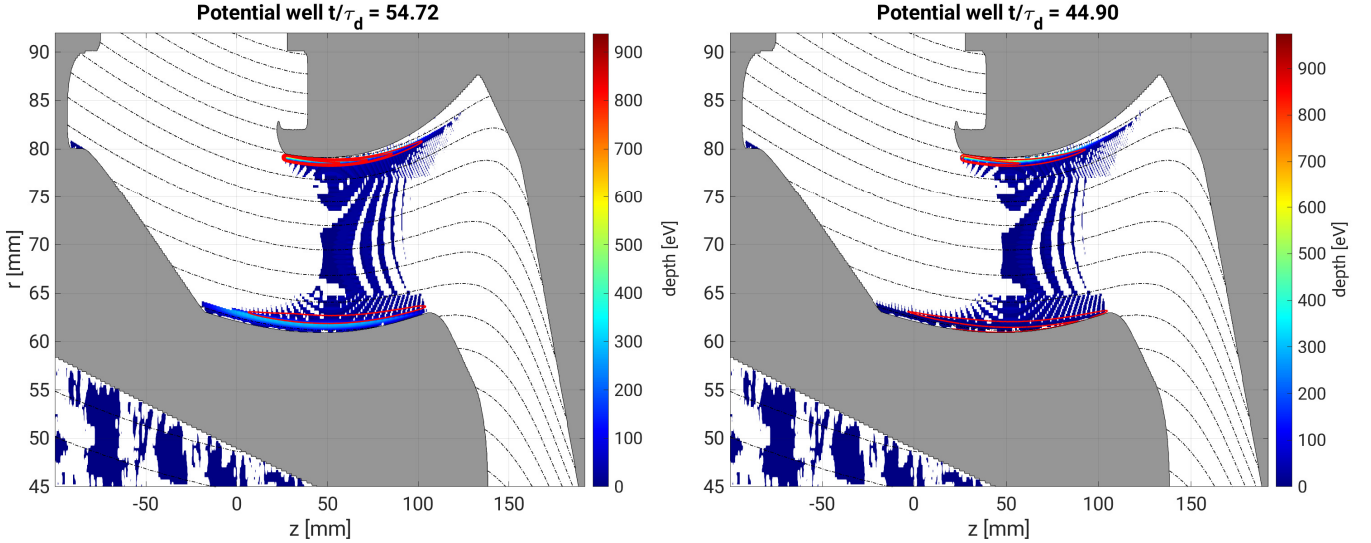


FIG. 31. Potential wells from Fig.(30), in presence of the electron clouds, in steady state. Some cloud density contours have been superimposed in red. Left: No IIEE. - Right: IIEE

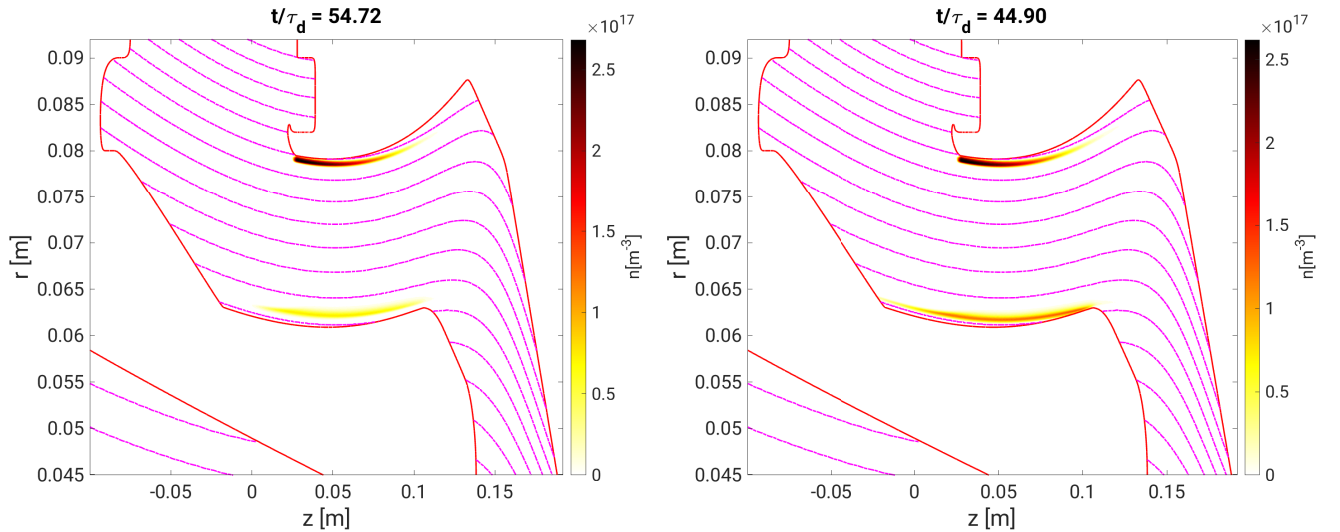


FIG. 32. Final cloud configurations and densities in both cases. Left: No IIEE. - Right: IIEE

The density plots from Fig.(32) enable to visualise the electrons repartition in the upper and the lower wells. In the case without IIEE, the lower well is much less filled. The exact density difference can not be extracted from the colorbar at naked eye, hence, the peak densities in both clouds are shown as time evolving variables on the current-plots Fig.(35-34). The density in the lower cloud with IIEE is about two times the one without.

With these informations in hand, let us now focus on the electric currents flowing in the vacuum chamber. The currents measured at each boundary of the MIG over time have been reported on Fig.(35-34). The time has been normalised by the collision time so the two situations can be compared. In absence of ion-induced emissions, three components contribute to the current measure between the cathode and the grounded regions. The green curve shows the current from electrons leaving the lower cloud. The red curve corresponds to the electrons leaking from the upper cloud and being captured at the anode. Some of them are captured in the cloud region, and some are captured when hitting the wall as they follow magnetic lines towards the exit of the MIG (see current densities in Fig.(36)). The dashed, light blue curve shows the ionic current produced as the ions flow towards the cathode. The total current is plotted in solid black. The dashed black curve is the sum of all current contributions considering IIEE.

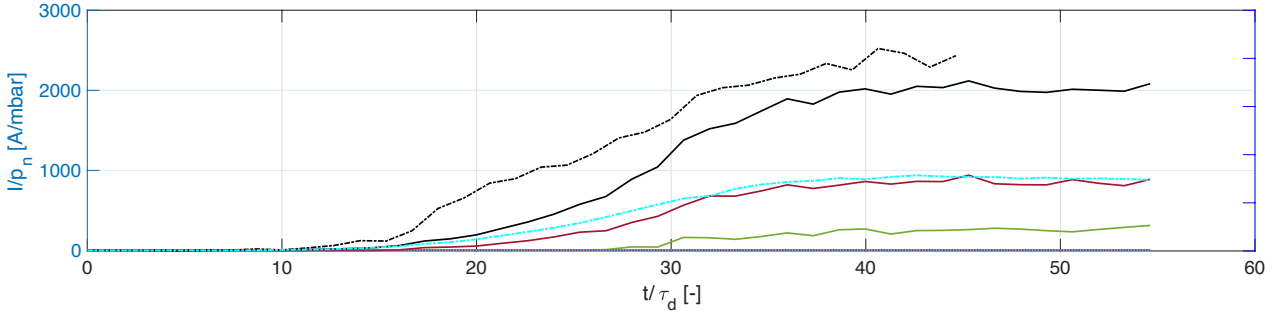


FIG. 33. Top: Evolution of all the current components inside the MIG, without ion-induced emissions. The color code corresponds to the domain boundaries highlighted in Fig.(34). The dashed black curve corresponds to the total current with IIEE. Bottom left: All current components without IIEE, in steady state. - Bottom right: same with ion-induced electrons.

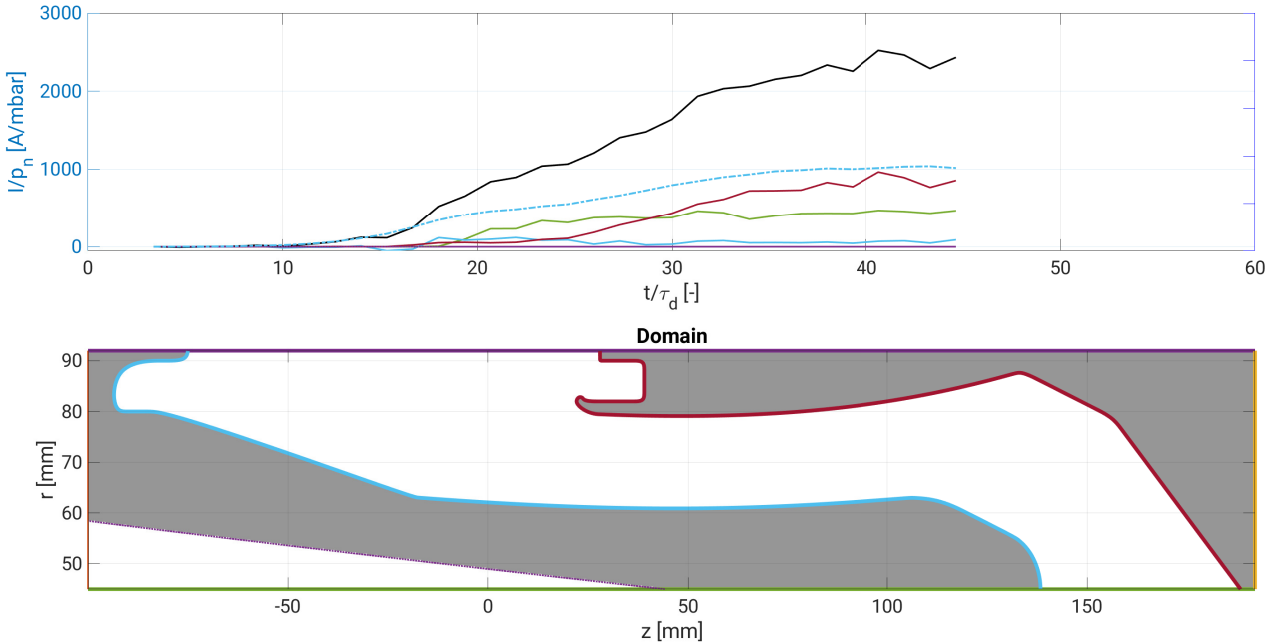


FIG. 34. All measured current contributions, in presence of ion-induced electron emissions, and represented over the normalised time.

Considering ion-induced electron emissions, the total current measured is higher. Indeed, as showed in Fig.(34), there is a higher contribution at the exit of the MIG chamber (green curve), as well as a slightly increased ionic current (dashed light blue). The current collected at the surface of the anode is identical, since this is only influenced through the upper cloud behavior, as explained when dealing with the slanted TREX geometry. The solid light blue curve corresponds to the electrons collected at the cathode surface, after being emitted by ions in that region. They do not contribute to an additional current since they tend to decrease the ionic one. So the total current (solid black line) is given by the sum of the red, the green, and the dashed light blue curves minus the solid light blue one. The difference in the magnitude of each current contribution, with and without IIEE, can be seen on the plots from Fig.(35), below. On the latter, the lower cloud densities are shown with the solid, dark blue lines, while the upper cloud densities, identical, are given by the dashed, dark blue lines. One has to read the densities on the right vertical axis.

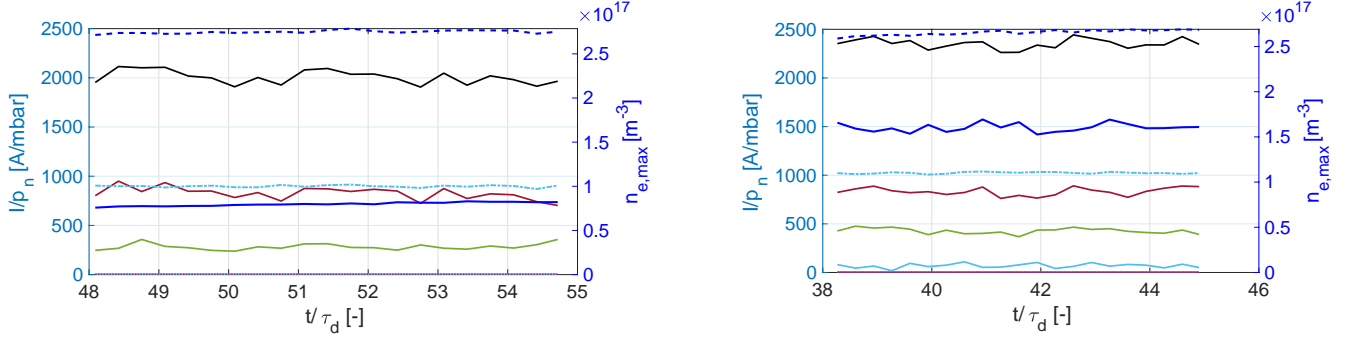


FIG. 35. Steady state current components inside the MIG, without (left) and with (right) ion-induced emissions. The color code corresponds to the domain boundaries highlighted in Fig.(34). The solid dark blue lines are for the lower cloud densities and the dashed one for the bottom clouds.

Introduced before as a tool to measure which are the main contributions to the currents collected at the domain boundaries, the current densities for both electrons and ions are shown on Fig.(36). The current densities are measured in steady state.

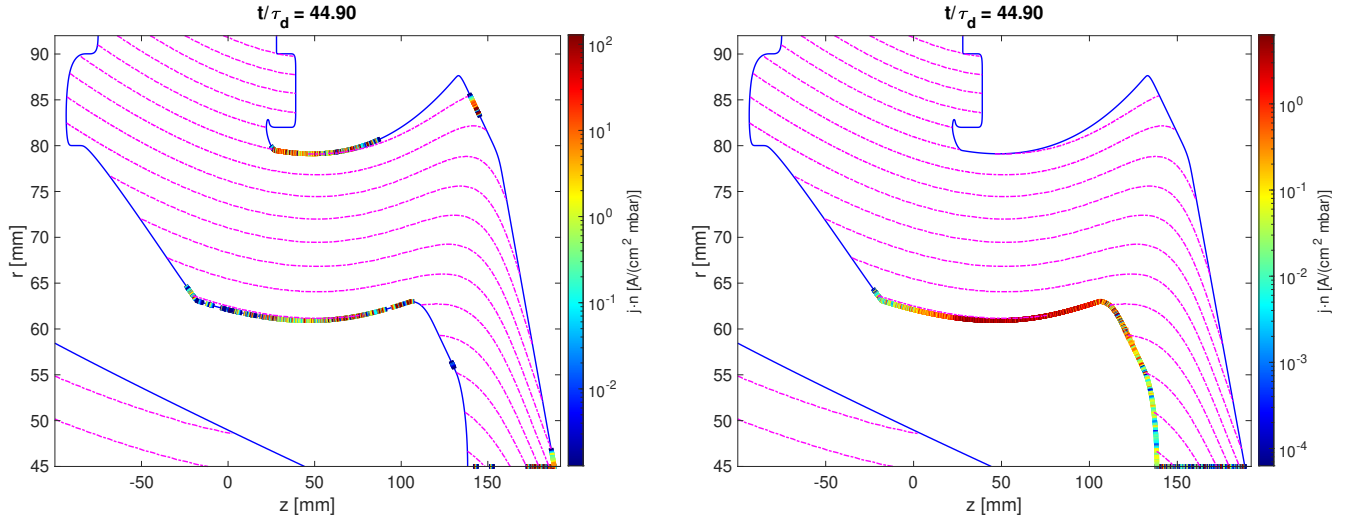


FIG. 36. Current densities for both electrons (left) and ions (right), in steady state and with IIEE.

As to sum things up regarding this comparative case study in the GT-170 geometry, results were as predicted at the end of TREX results, a combination of the ones obtained in slanted and in extrude geometries. The clouds' densities were affected, as the bottom cloud was filled with more electrons generated around its trapping region. The currents were affected too. The total collected current got increased of about 20% in steady state, increasing the pressure on the power supply needed for the MIG. Moreover, as the ionic current density is non zero (although very low) at the end of the cathode (see Fig.(36) - right), some electrons are produced in this region, and might be adiabatically trapped in

the domain [PPZ<sup>+</sup>16]. This could result in some more disturbance, but this effect will not be treated in this document.

### C. Further implementation

As of now, the module implemented in the FENNECS code to deal with ion-induced electron emissions does not take account for some physical features and parameters, and one could consider adding them to code. For example, the angular dependance on the yield model has been mentioned but not implemented. In fact, the yield is supposed to depend on two angular parameters. The angle of the ion beam with respect to the surface normal, and the emission angle of the electrons. The two dependences are stated below and could be used to complement the existing module. Let us denote by  $\theta_i$  the angle of ions with respect to the surface normal ( $\theta_i = 0$ ) and  $\theta_e$  the escape angle of electrons. If the ion beam is tilted by an angle  $\theta_i$ , the path-length of the incident particles in the electrons escape zone is prolonged by a factor of  $\cos(\theta_i)^{-1}$ . Hence, the total electron yield is supposed to be changed by

$$\gamma(E, \theta_i) = \gamma(E) \cdot \cos(\theta_i)^{-1}. \quad (17)$$

The previous equation is based on a straight ion path inside the solid. Experimentally, the term  $\cos(\theta_i)^{-1}$  was observed to behave as  $\cos(\theta_i)^{-f}$ ,  $0.5 \leq f \leq 1.5$  [DH]. The angular dependance of emitted electrons is expected to follow

$$\frac{d\gamma}{d\Omega}(\theta_e) = \frac{d\gamma}{d\Omega}(0) \cdot \cos \theta, \quad (18)$$

where  $\Omega$  denotes a solid angle around the emission direction.

## IV. CONCLUSION

In this report, different geometries have been introduced to study comparatively the electron cloud formation with or without ion-induced electron emissions, in magnetic potential wells. Only one kind of ions was used for the simulations, and the yield was implemented for ions impinging on aluminum only. These simulations were conducted while the TREX experiment is built, to help designing the latter, and to predict some of its results as well.

Results have shown that when the electrons were induced by ions in the trapping region, the cloud densities were affected, being in some cases, about twice as high as without ion-induced electrons. The density could only be increased in the cloud localised near the cathode, where ions impact. The formation times were shortened under considerations of IIEE, implying that the clouds can form faster, but still on the same time scale. Regarding the observed currents, since the difficulty to maintain the power supply raises with the current in the chamber, the effect of IIEE on the total collected current was investigated. In the end, it turned out that it could be increased by about 20%, confirming that the effect of IIEE is somewhat important. However, the order of magnitude of both the densities and the currents was preserved under considerations of IIEE. Thus, being costly to simulate, and their influence being moderate, they could be neglected when considering the formation of clouds in the design of power-supply devices to power gyrotrons.

## REFERENCES

- [Alb91] Stefano Alberti. Etude expérimentale de l'interaction faisceau d'électrons relativistes - onde électromagnétique dans un gyrotron quasi-optique. pages 2–5, 1991.
- [Bar93] Raúl A. Baragiola. Principles and mechanisms of ion induced electron emission. *Nuclear Instruments and Methods in Physics Research Section B: Beam Interactions with Materials and Atoms*, 78(1):223–238, 1993.
- [BLVV85] C.K. Birdsall, A.B. Langdon, J.P. Verboncoeur, and V. Vehedi. *Plasma Physics Via Computer Simulation*. Adam Hilger series on plasma physics. McGraw-Hill, 1985.
- [DAB<sup>+</sup>16] Caroline Darbos, Ferran Albajar, Tullio Bonicelli, Giuseppe Carannante, Mario Cavinato, Fabio Cismondi, Grigory Denisov, Daniela Farina, Mario Gagliardi, Franco Gandini, Thibault Gassmann, Timothy Goodman, Gregory Hanson, Mark A. Henderson, Ken Kajiwara, Karen McElhaney, Risto Nousiainen, Yasuhisa Oda, Toshimichi Omori, Alexander Oustinov, Darshankumar Parmar, Vladimir L. Popov, Dharmesh Purohit, Shambhu Laxmikanth Rao, David Rasmussen, Vipal Rathod, Dennis M. S. Ronden, Gabriella Saibene, Keishi Sakamoto, Filippo Sartori, Theo Scherer, Narinder Pal Singh, Dirk Strauß, and Koji Takahashi. Status of the iter electron cyclotron heating and current drive system. *Journal of Infrared, Millimeter, and Terahertz Waves*, 37(1):4–20, 2016.
- [DH] Karl-Ontjes Groeneveld Jürgen Kemmler Peter Varga Hannspeter Winter Dietmar Hasselkamp, Hermann Rothard, editor. *Particle Induced Electron Emission II*. Springer Berlin, Heidelberg.
- [Fis87] Nathaniel Fisch. Theory of current drive in plasmas. *Rev. Mod. Phys.*, 59:175–234, 01 1987.
- [Gen19] Jérémie Genoud. Advanced linear models for gyro-backward wave instabilities in gyrotrons. page 4, 2019.
- [Hag54] Homer D. Hagstrum. Theory of auger ejection of electrons from metals by ions. *Phys. Rev.*, 96:336–365, Oct 1954.
- [HGA<sup>+</sup>09] J.-P. Hogge, T. P. Goodman, S. Alberti, F. Albajar, K. A. Avramides, P. Benin, S. Bethuys, W. Bin, T. Bonicelli, A. Bruschi, S. Cirant, E. Droz, O. Dumbrajs, D. Fasel, F. Gandini, G. Gantenbein, S. Illy, S. Jawla, J. Jin, S. Kern, P. Lavanchy, C. LiÉvin, B. MarlÉtaz, P. Marmillod, A. Perez, B. Piosczyk, I. Pagonakis, L. Porte, T. Rzesnicki, U. Siravo, M. Thumm, and M. Q. Tran. First experimental results from the european union 2-mw coaxial cavity iter gyrotron prototype. *Fusion Science and Technology*, 55(2):204–212, 2009.
- [Jan82a] Joseph F. Janni. Energy loss, range, path length, time-of-flight, straggling, multiple scattering, and nuclear interaction probability: In two parts. part 1. for 63 compounds part 2. *Atomic Data and Nuclear Data Tables*, 27(2):147–339, 1982.
- [Jan82b] Joseph F. Janni. Energy loss, range, path length, time-of-flight, straggling, multiple scattering, and nuclear interaction probability: In two parts. part 1. for 63 compounds part 2. *Atomic Data and Nuclear Data Tables*, 27(4):341–529, 1982.
- [Kis73] L. M. Kishinevsky. Estimation of electron potential emission yield dependence on metal and ion parameters. *Radiation Effects*, 19(1):23–27, 1973.
- [LB22] Guillaume Le Bars. Models, manual and validations for fennecs code, 2022.
- [LBHL<sup>+</sup>22] G. Le Bars, J.-Ph. Hogge, J. Loizu, S. Alberti, F. Romano, and A. Cerfon. Self-consistent formation and steady-state characterization of trapped high-energy electron clouds in the presence of a neutral gas background. *Physics of Plasmas*, 29(8):082105, 2022.
- [OHA<sup>+</sup>11] T. Omori, M.A. Henderson, F. Albajar, S. Alberti, U. Baruah, T.S. Bigelow, B. Beckett, R. Bertizzolo, T. Bonicelli, A. Bruschi, J.B. Caughman, R. Chavan, S. Cirant, A. Collazos, D. Cox, C. Darbos, M.R. de Baar, G. Denisov, D. Farina, F. Gandini, T. Gassmann, T.P. Goodman, R. Heidinger, J.P. Hogge, S. Illy, O. Jean, J. Jin, K. Kajiwara, W. Kasperek, A. Kasugai, S. Kern, N. Kobayashi, H. Kumric, J.D. Landis, A. Moro, C. Nazare, Y. Oda, I. Pagonakis, B. Piosczyk, P. Platania, B. Plaum, E. Poli, Ł. Porte, D. Purohit, G. Ramponi, S.L. Rao, D.A. Rasmussen, D.M.S. Ronden, T. Rzesnicki, G. Saibene, K. Sakamoto, F. Sanchez, T. Scherer, M.A. Shapiro, C. Sozzi, P. Spaeh, D. Strauss, O. Sauter, K. Takahashi, R.J. Temkin, M. Thumm, M.Q. Tran, V.S. Udintsev, and H. Zohm. Overview of the iter ec hcd system and its capabilities. *Fusion Engineering and Design*, 86(6):951–954, 2011. Proceedings of the 26th Symposium of Fusion Technology (SOFT-26).
- [PPZ<sup>+</sup>16] Ioannis Gr. Pagonakis, Bernhard Piosczyk, Jianhua Zhang, Stefan Illy, Tomasz Rzesnicki, Jean-Philippe Hogge, Konstantinos Avramidis, Gerd Gantenbein, Manfred Thumm, and John Jelonnek. Electron trapping mechanisms in magnetron injection guns. *Physics of Plasmas*, 23(2):023105, 2016.
- [RAH<sup>+</sup>22] F Romano, S Alberti, J.P Hogge, J Genoud, G Le Bars, and J Loiozu. The trapped electrons experiment (t-rex). 2022.